CHALMERS
UNIVERSITY OF TECHNOLOGY

Effect of Ni-content on oxide scale microstructure of FeCr model alloys after breakaway corrosion at 600°C

Bachelor's thesis in

Marcus Brunström

Department of Energy and Materials
CHALMERS UNIVERSITY OF TECHNOLOGY
Gothenburg, Sweden 2018

Table of contents

Abstract 2

Introduction 3

Steel 4

Oxidation Theory 6
- Oxide formation 7
- Defects 7
- Diffusion 9
- Kinetics 9
- Corrosion Products 10

Analytical Techniques 12
- TG – Thermogravimetry 12
- SEM – Scanning electron microscopy 12
- EDX – Energy-dispersive X-ray spectroscopy 13
- BIB – Broad ion beam 13
- XRD – X-ray diffraction 13

Experimental 14
- Sample Preparation 14
- Exposure 14
- Cross sections 15

Results/Discussion 16
- Aim 16
- Non-exposed samples 16
- Exposed samples 20
- External results 28

Conclusion 31

Acknowledgments 32

References 33

Abstract

The world is presently enduring high amounts of greenhouse gases, thus the importance of finding eco-friendly alternatives for power production is growing for CO_2 emissions to be decreased. Combustion of biomass and waste is a sustainable alternative to the traditional fossil resources, although it faces some problems along with a lower efficiency. The combustion of biomass and waste creates a corrosive environment due to the heterogeneous composition which can be controlled if the temperature is kept low. If the propagation of the corrosion attack in a boiler for these sustainable resources can be better understood it could help select a cost-efficient alloy that can endure a higher temperature. This would make power production with biomass and waste better compare with the fossil resources in terms of electric efficiency.

For this purpose, Fe-18Cr-Ni model alloy coupons with varying Ni content (0-10%) were prepared, analyzed and subjected to exposure at 600°C in an aggressive environment to investigate the oxide microstructure after breakaway corrosion. Furthermore, an oxide thickness was chosen as a target for all alloys to facilitate the comparison of oxide microstructure. The conditions of exposure were 5% O_2, 95% N_2 with a 1 mg/cm^2 K_2CO_3 deposit on the samples. The oxidation times were calculated according to the intended oxide thickness. Comparable results from other studies with different conditions of exposure are also discussed. Analyzes were done by means of SEM, BIB, EDX, XRD and TG.

Samples were seen to show decreasing oxidation rate and mass gain with increasing amounts of Ni in this study. While the 5% Ni alloy showed relatively long incubation time, the 10% Ni alloy showed none which indicates a stable oxide growth for content around 10%. A stable oxide growth could be seen in the austenitic alloys, this could be seen in a 10% Ni sample but partly also in the 5% Ni sample. Replicating an oxide thickness acquired in the TG proved to be difficult due to differences in the equipment and deviations in combination with incubation time. Good performance of the austenitic alloys is seen but seemingly this is temperature dependent and ferritic alloys will perform better at 800°C.

Introduction

With the environment presently enduring high increases in greenhouse gases it is important to use more sources of power production that is of sustainable character to decrease CO_2 emissions [1]. Power production through combustion of non-fossil resources, such as biomass and waste, is a promising alternative although it faces some problems. The main issue is the heterogeneous composition of biomass and waste which contains considerable amounts of alkali and chloride compounds, these are known for accelerating corrosion towards the metallic parts of the boiler [2-7]. In order to prevent substantial corrosion damage, the temperature is usually kept below 450°C. By combusting biomass and waste at a higher temperature the generated power would increase but even more the degradation of the boiler [5,8]. Although combustion of fossil fuels is more efficient than non-fossil fuels, increasing the corrosion resistance in the boiler could help alternative-fuel type of power production better compare with fossil types, since the life-time of the boiler would increase [4,9]. Therefore, a better understanding the corrosion mechanisms in this environment could help select cost efficient alloys for waste fired boilers which would promote the use of alternative fuels for power production. Low alloys and stainless steels are the ones commonly used in waste fired boilers, these form different oxides depending on composition and environment. Stainless steels rely on the Cr-rich oxides as protective layers (primary protection), when these steels are exposed to the aggressive environment, produced during the combustion of biomass and waste, a tendency to suffer from breakaway corrosion is observed [7,10]. After breakaway of the protective Cr-rich oxide a less protective Fe-rich oxide will form along with a spinel oxide, this leads to accelerated corrosion rate [10,11]. Once this effect has taken place the corrosion resistance of the steel relies on these remaining oxides [11].

Besides Cr, other elements can be added to stainless steels to achieve different properties, eg. Ni, Mn, Nb, etc. The addition of Ni to steel common for the austenitic stainless steels since Ni broadens the range of which the austenite phase is present and stabilizes it. The spinel oxide inherits the composition of the steel, thus the addition of Ni can be varied to investigate how this affects the oxide microstructure and the corrosion resistance. In order to investigate and better understand the effects of Ni on the oxides microstructure and the propagation of a corrosion attack, an alkali compound (K_2CO_3) could be deposited on the model alloy (Fe-Cr-Ni) before exposure. This helps to deplete the Cr-rich oxide surface and create the Fe-rich and spinel oxide (secondary protection) that are present in an active waste fired boiler as exposure is performed. Different analytical methods can be applied before and after this exposure to gain information about the formation and behavior of these oxides. The aim of this study is to investigate the effect of Ni on the secondary protection of Fe-Cr-Ni model alloys by exposures at 600°C in presence of K_2CO_3 to simulate the aggressive environment of a waste fired boiler.

Steel

Generally, steel is an iron and carbon alloy where carbon is used to enhance the mechanical properties of the iron. Other elements can also be added for steel to receive different characteristics e.g. chromium can be added to the steel to increase its corrosion resistance [12]. In order to be classified a steel as stainless steel the chromium content needs to be at least 11% [13]. However, at the boiler operating temperatures carbon reacts with the chromium producing chromium carbides which have negative effect on the corrosion resistance [14]. In order to avoid this, alloys with low carbon content are used for boilers [14]. The alloys used for this study are model alloys which do not contain many of the common elements found in commercial steels such as C, Mn, Nb, Si, etc. but only Fe, Cr, Ni and very low amounts of Al [15], the composition of the model alloys can be seen in table 1. By using a Fe-Cr-Ni model alloy the potential effects on corrosion resistance that other elements of the commercial steel can have, this facilitates the interpretation of the results of the effects of Ni.

Nr.	**Cr**	**Ni**	**Al**
1	**18**	*	*
8	**18**	10	0.005
10	**18**	5	*

*<0.01 Wt%

Table 1: Tested model alloys composition.

There are several different phases that steel can adopt depending on composition and temperature. The phases present at the temperature and composition variation of this study are ferrite (δ) and austenite (γ), this can be seen in figure 1. Ni is an element known to broaden the range of which austenite is present and to stabilize it. Thus, austenite can be found at lower temperatures for steels with Ni content. The addition of Cr on the other hand promotes the ferrite phase in the steel [13]. These effects can partly also be seen in figure 1. Ferrite has a crystalline structure that is body centered cubic (bcc) and austenite a face centered cubic (fcc), illustrations of these can be seen in figure 2. The crystals formed in metals are called grains. The size of these are dependent on the microstructure and temperature [16].

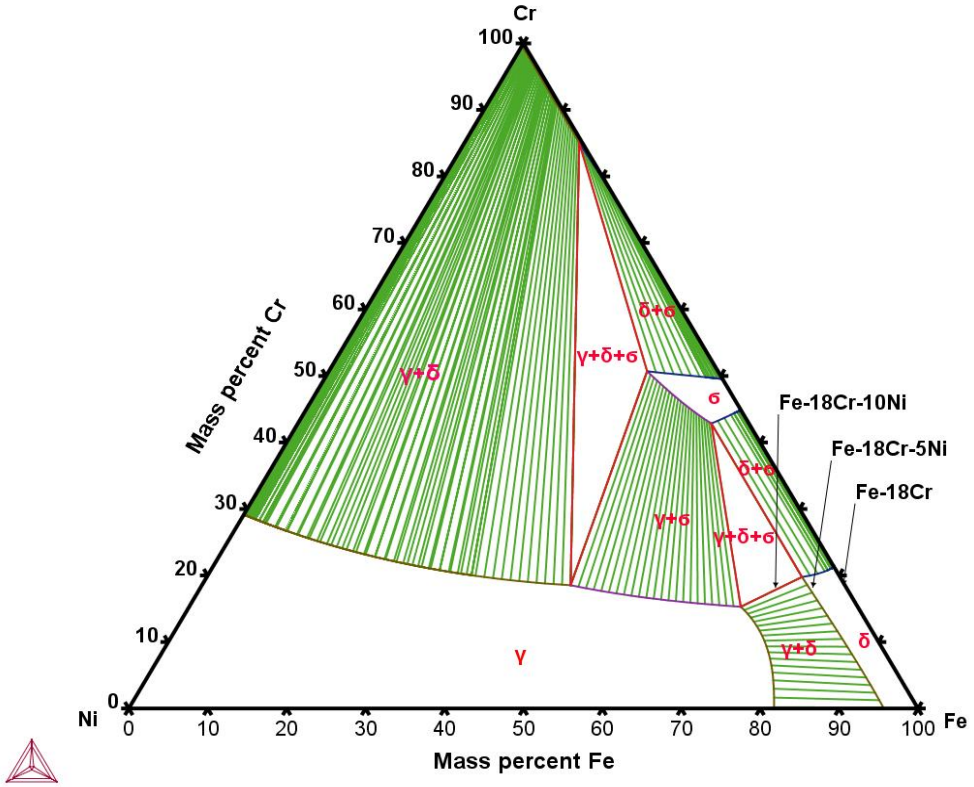

Figure 1: Isothermal ternary phase diagram for 600°C created with Thermo-Calc software using TCBIN database [17]. The model alloys from table 1 are marked. The ferrite region is marked δ and the austenite γ.

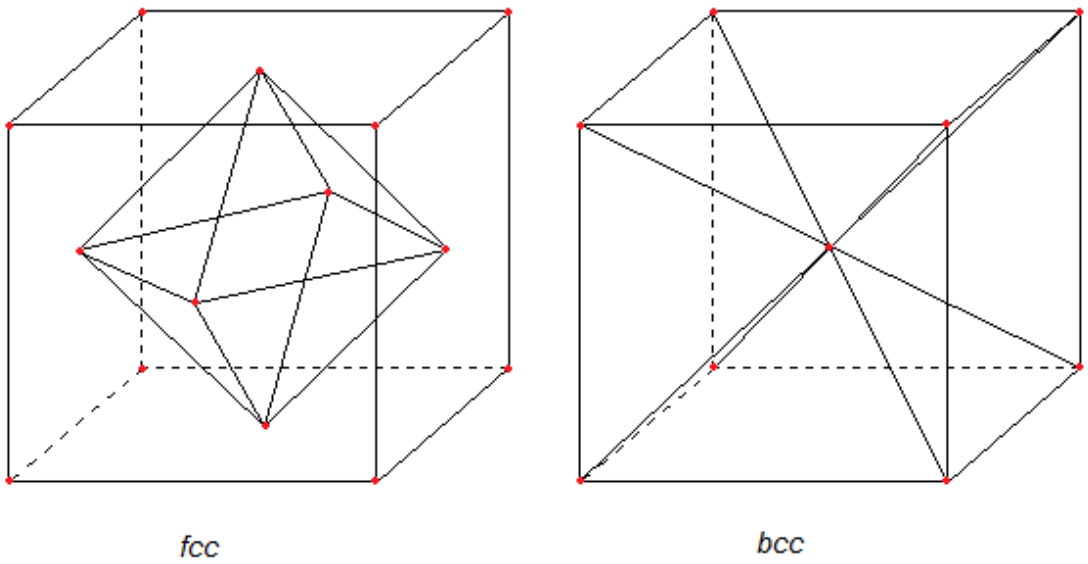

Figure 2: Unit cells for fcc and bcc, red dots at the corners represent the center of an atom.

Oxidation theory

Metals (*M*) are generally thermodynamically unstable in environments containing oxygen and are thus likely to react and form metal oxides, e.g. reaction 1.

Reaction 1: $xM(s) + (y/2)O_2(g) \rightarrow M_xO_y(s)$

The thermodynamic condition for this is that the partial pressure of the oxygen is greater than the dissociation pressure of the oxide ($pO_{2,environment} > pO_{2,\ dissociation}$) [18,19]. Gibbs law of free energy can also be applied to see if a reaction is spontaneous [20], see equation 1.

Equation 1: $$\Delta G = \Delta G^\circ + RT\ ln\left(\frac{aMxOy^{2/y}}{(aM^{2x/y})(aO2)}\right)$$

Here *R* is the gas constant and a represent the activities of the reaction reactants and products. If Gibbs free energy is negative ($\Delta G < 0$) the reaction is spontaneous [18]. Gibbs law also provides information about the stability of the oxides. If it is set to express equilibrium (i.e. $\Delta G = 0$) it can be plotted to receive an Ellingham diagram which can be used to predict the oxidation or reduction of a metal at different temperatures, see figure 3.

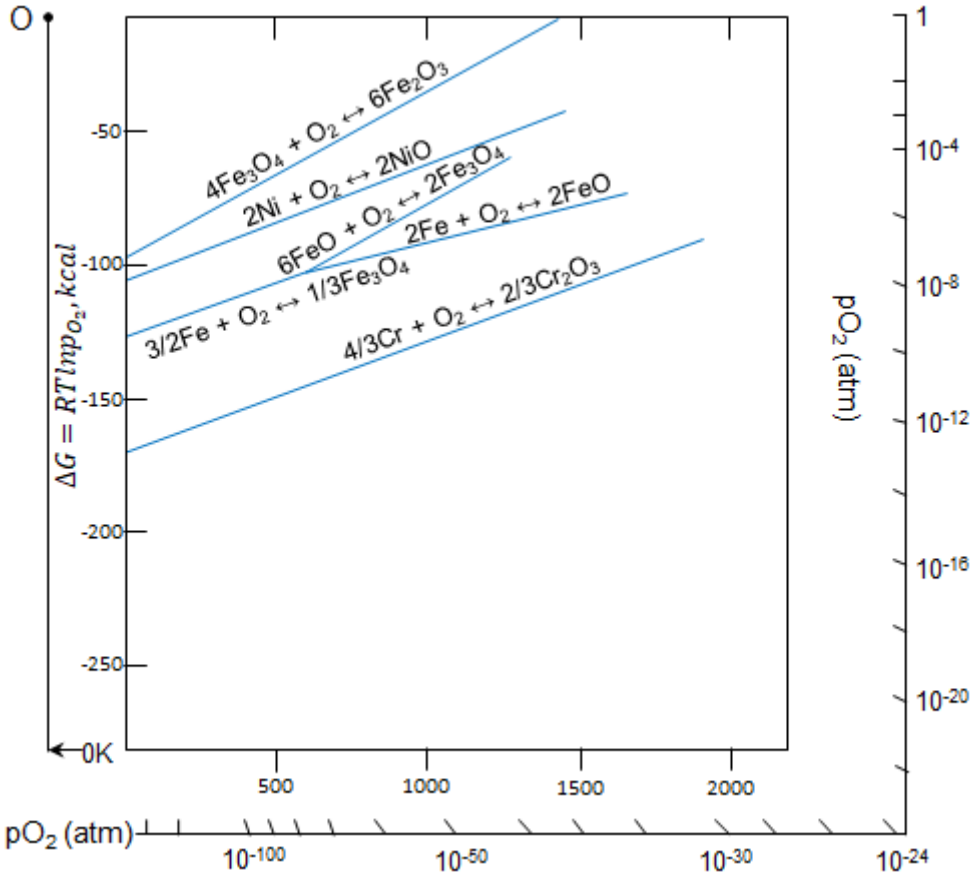

Figure 3: Ellingham diagram. Based on [22].

Oxide formation

When a metal oxide is formed oxygen is adsorbed to the surface and reduced by the cations in the metal. Once the oxide nuclei have formed and the oxide grew to cover the surface, the metal and gas are no longer in direct contact. Hence continued oxide growth is determined by diffusion through the oxide scale [21]. However, cracks in the scale can occur which restores direct contact between gas and metal, this accelerates oxide growth [22]. The diffusion through the oxide is enabled by several things, electric fields, chemical potential gradient and defects.

Defects

The presence of defects in the metal and oxide allows diffusion to occur. These defects can be voids, pores or cracks and can be classified as either point defects or line and surface defects [22,23]. The point defects are single lattice location defects such as vacancies and interstitials. The Schottky and Frenkel defects are described using these and appear in order to balance charge in the material. The Schottky defect consists of a cationic vacancy along with an anionic one and an interstitial cation as well as a cationic vacancy is called the Frenkel defect, see figure 4.

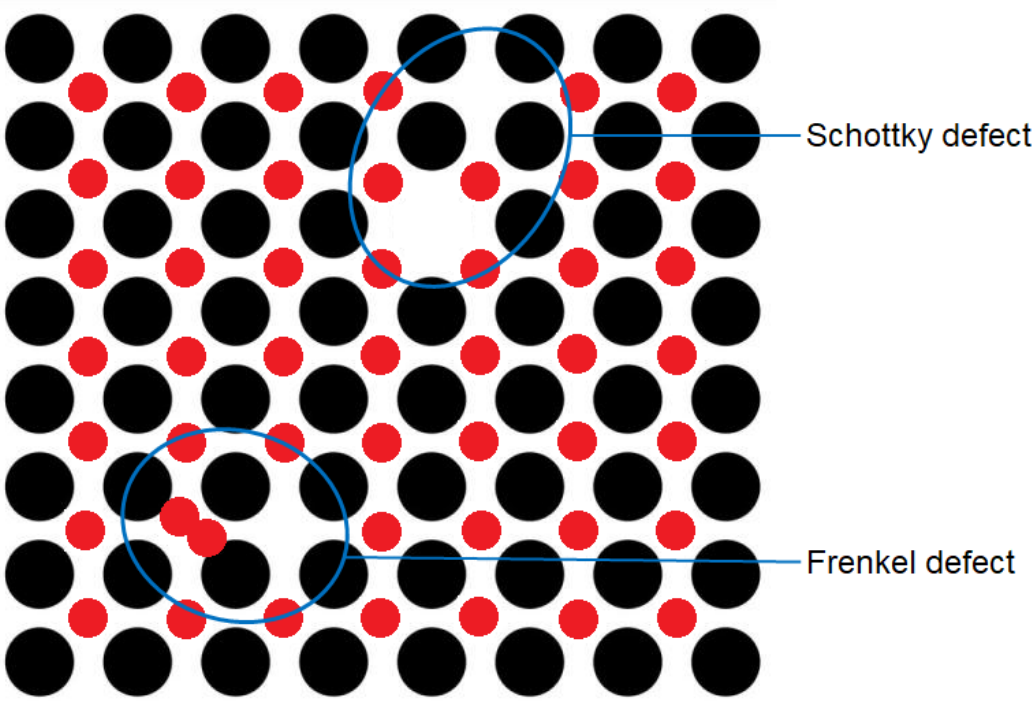

Figure 4: Illustration of the Schottky and Frenkel defects.

Defects such as grain boundaries, dislocations and inner and outer surfaces are classified as line and surface defects. Ideally steel would have only one crystal, however in reality many grains are formed. The grains can have the same crystalline structure but different orientation, thus being separated. The border where a crystal meets another are called grain boundaries e.g. figure 5. Dislocations are atoms that are out of position in the crystal, illustrations of this can be seen in figure 6.

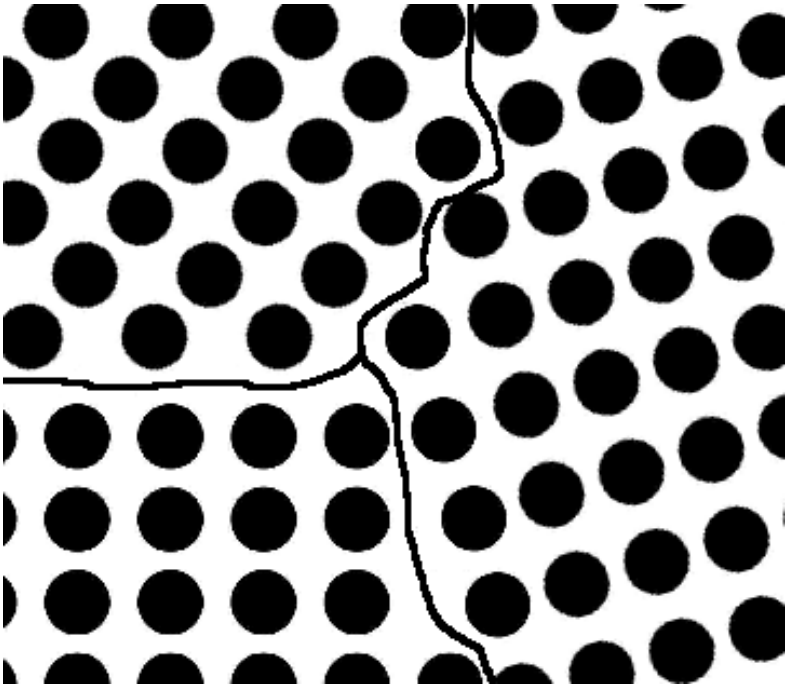

Figure 5: Illustration of grain boundaries between 3 grains in 2 dimensions.

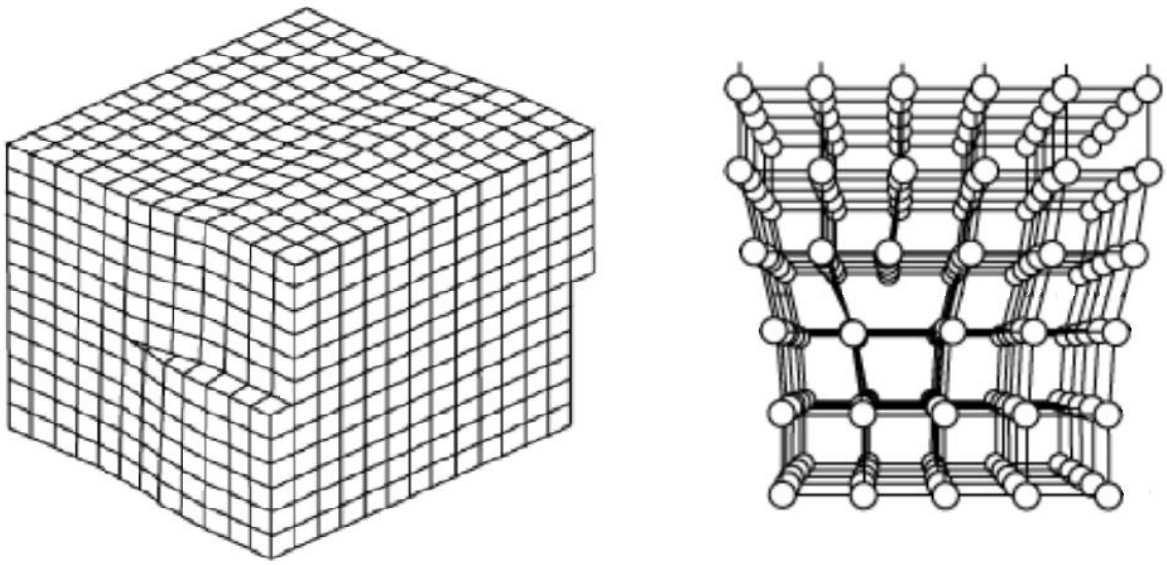

Figure 6: Illustrations of dislocations [24].

Diffusion

Diffusion allows for transport of oxygen as well as metal through the material defects, i.e. diffusion occurs both inwards and outwards in the oxide. In a study by Atkinson and Taylor, the diffusion mechanisms of metal are stated to be applicable for metal oxides as well [25]. Diffusion can be classified as either lattice type (bulk) or short-circuit type depending on the type of defect that is used for transport through the material [22]. The lattice diffusion is enabled by the point defects and allow movement of ions and atoms through the bulk of the material. This diffusion type is important for higher temperatures but around lower temperatures, e.g. 600°C as used in this study, the most important diffusion is the short-circuit type since it has a lower activation energy [22]. The line and surface defects are what causes short-circuit type diffusion. Since grain boundaries are short-circuit diffusion paths that means grain size have effect on the diffusion. Smaller grains create more boundaries thus also more diffusion paths. As a result of this the Cr diffusion in the material is affected by the grain size which can affect the corrosion resistance of the metal. So, the same alloy with different grain size can generate different results [26].

Kinetics

Thermodynamics gives an idea of what reactions are favorable to occur but cannot predict which ones will or at what rate [19]. The oxidation kinetics can be read from a mass change curve of a sample. Oxidation follows three kinetic laws, linear, parabolic and logarithmic, an illustration of these can be seen in figure 7. Since the kinetic laws are directly connected to the oxidation rate they are affected by the same factors i.e. temperature, time, oxygen partial pressure, surface preparation and material pre-treatment.

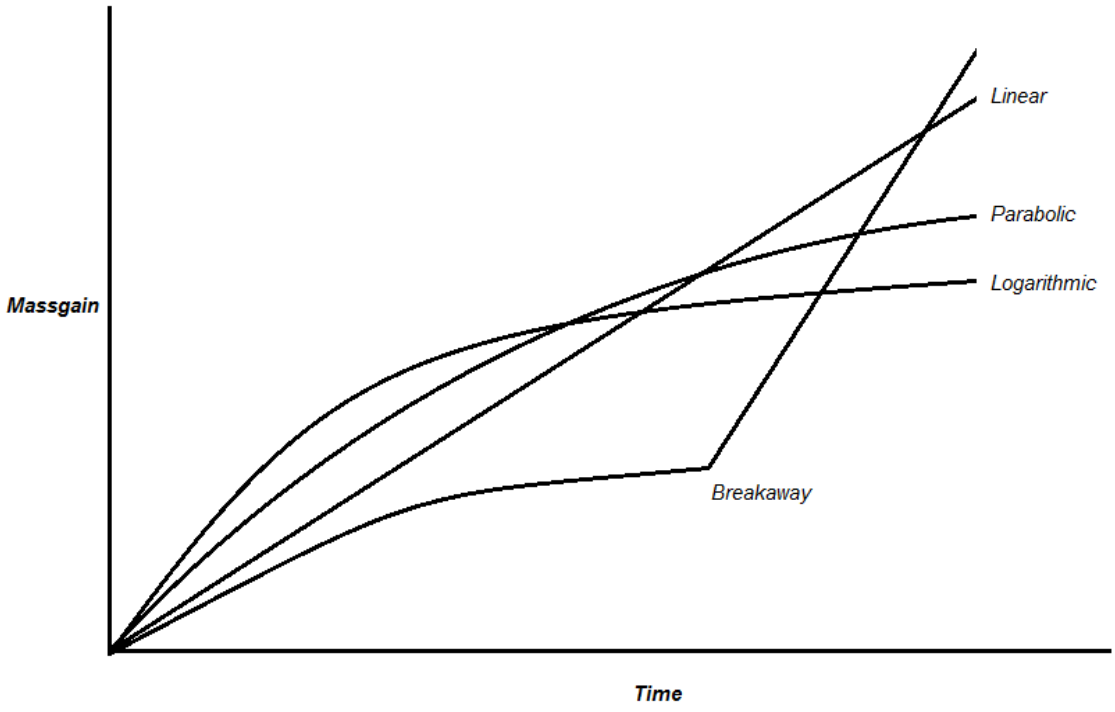

Figure 7: Kinetic laws for oxidation.

Linear rate law

The linear rate law is expressed with equation 2 and describes a constant oxidation rate over time. This type of growth rate is determined by surface or phase boundary reactions and is common in early stages of an oxidation [18].

In the following equations x is the oxide thickness, K_{index} are rate constants, t is time and A-D are constants.

Equation 2: $x = K_L t + A$

Parabolic rate law

The parabolic rate law is common for metals in high temperature oxidation and is expressed by Wagner with equation 3 [27,28]. It is limited by the transport of ions and electrons through the oxide scale, thus the growth rate is reduced as the oxide thickness increases.

Equation 3: $x^2 = K_P t + B$

Logarithmic rate law

Oxide growth that follows the logarithmic rate law occurs at temperatures up to 400°C and has an initially high rate which decelerates over time [20,27]. It can be expressed with as direct logarithmic with equation 4 or as inverse logarithmic with equation 5. The factors that the logarithmic law is driven by remains to be determined.

Equation 4: $x = K_{Log} Log(t + t_0) + C$
Equation 5: $1/x = D - K_{iLog} Log\ t$

Breakaway corrosion

Oxidation rate does not need to behave only according to one kinetic law, breakaway or catastrophic corrosion is an example of this. The oxidation rate initially behaves parabolically or logarithmically but is then accelerated after time and adopts a rapid oxidation rate. This effect is driven by cracks and pores formed in the oxide [20].

Corrosion products

When the metal reacts with oxygen different oxides can form which have different content and properties. The oxides also have different formation rates and protection. The oxide can be considered protective if the oxidizing agents access to the metal through the oxide is determining the rate of oxidation [14]. To consider an oxide as protective it should fulfill the following characteristics [18].

- Thermodynamically stable
- Diffusion coefficient for metal ions and oxygen should be low
- Similar thermal expansion coefficients of oxide and metal
- High melting temperature
- Full adherence to the substrate
- High plasticity at high temperature

The protective properties Cr gives steel comes from the formation of protective Cr-rich oxide (Cr_2O_3). The Cr-rich oxide scale provides the primary protection of the steel, however the corrosive alkali compounds present in the boiler environments are known to deplete the Cr [7,12]. Hence a simulation of the boilers environment can be performed by depositing K_2CO_3 on the metal resulting in depletion of the Cr and breakaway of the primary protection. The mechanisms for this is shown in reaction 2 [29].

Reaction 2: $1/2Cr_2O_3(s) + K_2CO_3(s) + 3/4O_2(g) \leftrightarrow K_2CrO_4(s) + CO_2(g)$

When the Cr is depleted no new full protective Cr-rich oxide scale is formed since the formation of it is a slow process [22]. After the Cr depletion, the oxidation rate is accelerated, this is when breakaway corrosion is seen for the steel [19]. After breakaway the corrosion resistance of the steel relies on the secondary protection, that is investigated in this study, which is less protective and consists of hematite and a spinel oxide [10,11]. The hematite is an Fe-rich oxide (Fe_2O_3) which grows outwards. The spinel oxide is inwards growing with the following composition $(Fe,Cr,Ni)_3O_4$ [30]

Analytical techniques

In order to collect information about the behavior of the samples during the experimental procedure different analytical techniques were used. Interpreting and connecting results from the different methods is a good way to understand the effects and mechanisms taking place and enables a better assessment of the samples.

TG - Thermogravimetry

The thermogravitry (TG) is a technique where the weight change of a sample is measured over time, with µg precision, whilst subjected to pre-set heat and atmosphere conditions in a furnace [31]. The weight change curves generated can be normalized to the surface area of the sample to give information about the rate of oxidation of the alloy. The instrument used for this work was a SETARAM SETSYS Evolution TGA.

SEM - Scanning electron microscopy

The scanning electron microscope (SEM) utilizes a beam of electrons to scan the surface of a sample. The electrons interact with the surface producing different signals e.g. backscatter and secondary electrons, see figure 8 [32]. Detectors in the SEM then pick up signals from the interaction to create an image with high resolution and magnification potential [32]. For this study a backscatter detector was used. Performing this analysis provides good information about the microstructure of the sample. For plan view a Phenom Pro X desktop SEM was used and for cross section a FEI Quanta 200 ESEM.

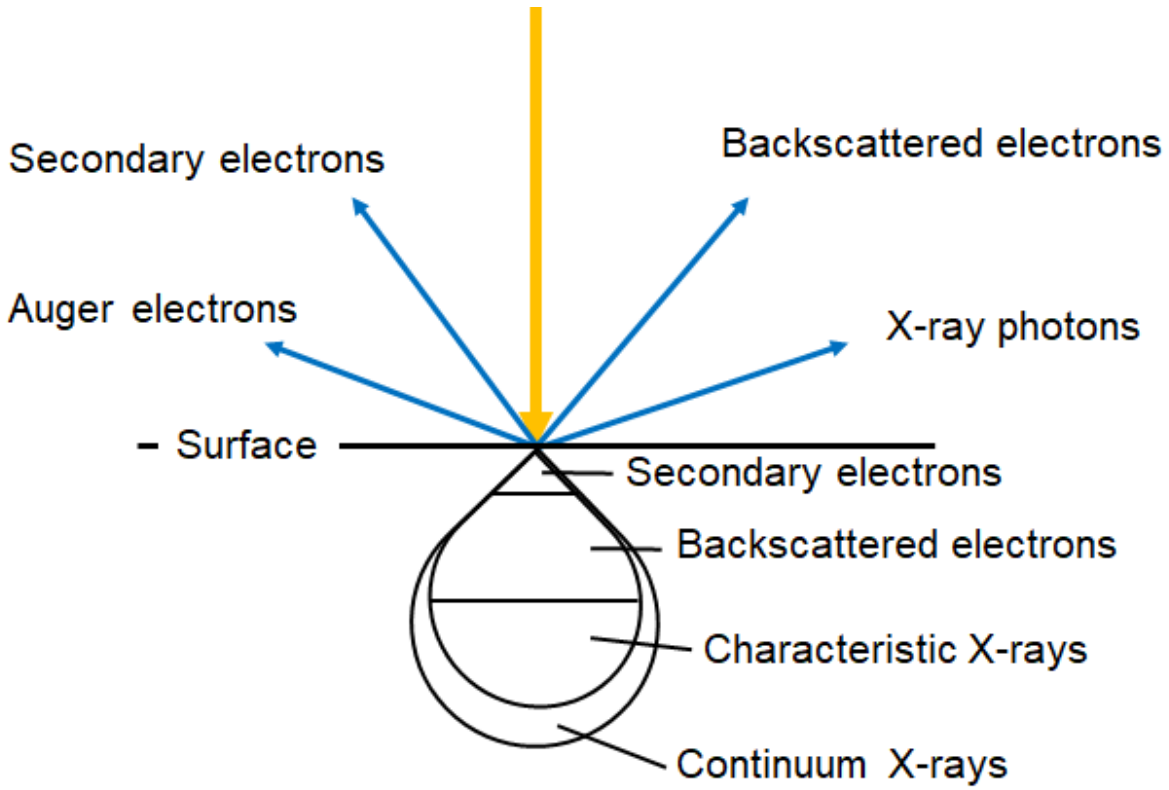

Figure 8: Electron beam interaction with a surface.

EDX - Energy-dispersive X-ray spectroscopy

The SEM can also perform an element analysis of the sample by detecting X-rays emitted from the surface through excitation if equipped with an instrument for energy-dispersive X-ray spectroscopy (EDX). Excitation of electrons generate characteristic X-rays for elements which can be identified by the detector to give information about the chemical composition of the sample [33]. The Phenom Pro X desktop SEM used for plan view is also equipped with an EDX allowing for elements to be analyzed along with the plan view. For cross section an Oxford X-max 80 EDX was used.

BIB - Broad ion beam

The Broad ion beam (BIB) is used to prepare a sample for cross section. It does this by launching argon ions from three cannons with different angles towards the sample milling it to precise smoothness [34]. To define the area of milling, the sample was placed behind a titanium mask allowing the BIB to target what is not covered behind the mask. A polished surface created by the BIB can be imaged and analyzed in the SEM for valuable information about the propagation of the corrosion attack as well as the microstructure. A Leica TIC 3X BIB was used.

XRD - X-ray diffraction

X-ray diffraction (XRD) is used to identify different crystalline phases in a sample using Bragg's law as can be seen in equation 6 [35]. A cannon launches X-rays with a fixed angle towards the sample which interacts with its surface. The angle of which the X-rays leave the surface gives information about the phases present in the sample since the leaving angle depends on the X-rays interaction with the surface [35]. The phases can then be identified by comparing the generated results with a database of known crystalline compounds. For this analysis a Siemens diffractometer D5000 was used.

Equation 6: $n\lambda = 2d\,Sin\theta$

Here n is a positive constant, λ the wavelength, d the interplanar distance and θ the angle.

Experimental work

Sample preparation

All tests were done on model alloy coupons with the composition according to table 1 and the dimensions of 10 x 8 x 2 mm with a 1 mm diameter drilled hole to facilitate the handling of the samples. In order for the alloys to be comparable all samples underwent the same preparation process. Initially the samples were heat treated at 950°C for 1 hour to relieve the grains of potential mechanical stresses that could affect the corrosion behavior. The heat-treated samples were then grinded and polished in automatic rotating grinders for even surfaces. The samples sides were grinded by hand using a Struers RotoPol-31 grinder with 1000 SiC abrasive paper and water as lubricant until smooth. The front and back of the sample was grinded and polished in 4 steps according to table 2 to achieve a mirror like surface in a Struers TegraPol-31 grinder.

Nr.	Paper	Polish suspension	Lubricant
1	500 SiC	*	Water
2	9 µm	*	Dp-lubricant yellow
3	3 µm	Dp-suspension A 3 µm	Dp-lubricant yellow
4	1 µm	Dp-suspension A 1µm	Dp-lubricant yellow

Table 2: All products used for grinding are Struers products associated with the machines.

Between each step the samples were rinsed with distilled water in order to remove particles, polish suspension and lubricant from the previous step. After polish the samples were cleaned in an ultrasonic bath with acetone for 10 minutes followed by ethanol for 10 minutes, both at a temperature between 25-35°C. Each sample was cleaned in individual containers in ultrasonic bath. The prepared samples were then stored in plastic containers, that were washed with ethanol, until testing.

Exposure

Prior all exposures samples were sprayed evenly with a solution of saturated K_2CO_3(s) in 80/20 ethanol-water using nitrogen gas. Samples were placed in a holder to fix the position when spraying, a constant flow of hot air was used to dry the applied salt. Samples were weighed using a Mettler Toledo xp26 scale with 6 decimals precision before and after spraying to ensure obtaining the desired coverage. All samples were sprayed to 1 mg/cm^2 K_2CO_3. The sprayed samples were then exposed in the TG or a tube furnace. The tube furnace was set to have a gas flow of 2.5 cm/s (1000 mL/min) 5% O_2 and 95% N_2 and a temperature of 600°C, this temperature was calibrated using an external thermocouple.

All samples were weighed again after heat treatment in the tube furnace for mass gain and oxide thickness to be calculated. For the TG exposures the gas composition and temperature was set to be the same as for the tube furnace, however the gas flow is lower in the TG.

Cross section

In order to prepare samples for cross section the samples were first covered with a thin layer of gold using a sputtering machine. This was done to be able to distinguish in the SEM the sample from the Si-wafer which was glued to the sample to protect the oxide. To acquire cross section images the samples were first cut by a Struers Minitom low speed diamond saw. Samples were then milled with the BIB to reveal the microstructures of the metal for the SEM to analyze.

Result/Discussion

Aim

The purpose of this study is to investigate the effect of Ni on the oxidation of Fe-Cr alloys in aggressive environment at 600°C. The different model alloys were analyzed and tested with different methods to understand this effect. For comparison, a specific oxide thickness was chosen to examine the alloys at the same oxidation stage.

Non-exposed samples

In order to understand the results from the exposed samples and the propagation of the corrosion attacks on them it is necessary to have knowledge about the original samples. Microstructure examination on unexposed model alloys was performed by means of SEM but was firstly etched, with a solution of 45vol% HNO_3, 10vol% HCl and 45vol% water, in order to reveal the microstructure phases. A SEM image of a sprayed sample was done to observe the distribution of salt over the surface of the sample as well as to facilitate identification of the salt in SEM images of exposed samples, this can be seen in figure 9. The microstructure of the different model alloys can be seen in their respective SEM images seen in figures 10, 11 and 12. The size of the grains can be estimated from these images. XRD was used to confirm the model alloys phases according to their chemical compositions and microstructures. The diffractograms of these analyzes can be seen in figures 13, 14, 15. Microstructure and XRD results from non-exposed samples are compiled in table 3.

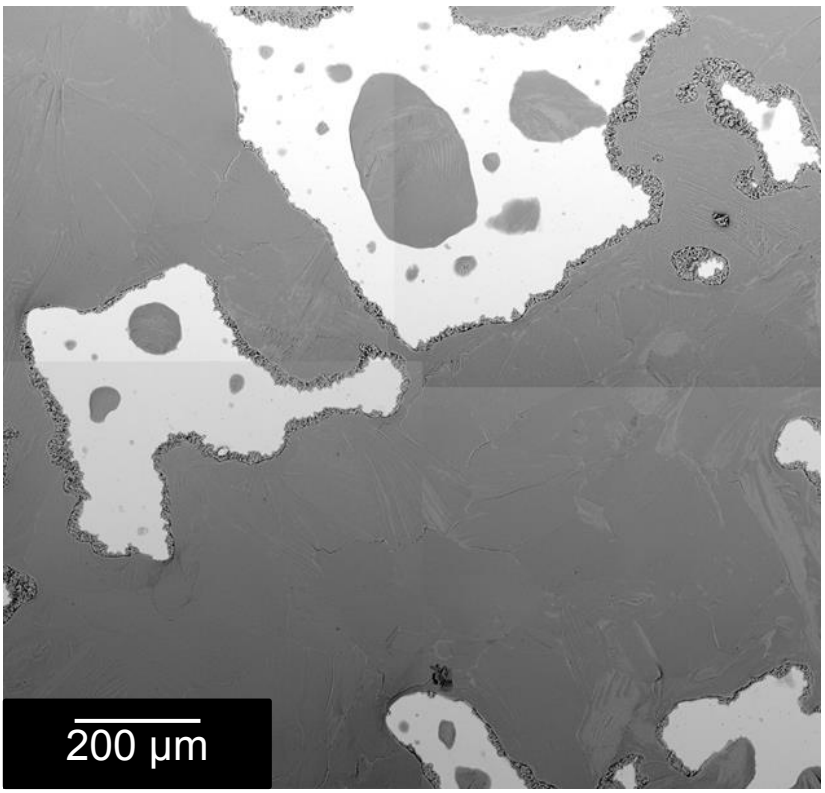

Figure 9: Grouped SEM images of a non-exposed sample sprayed to 1mg/cm^2 K_2CO_3

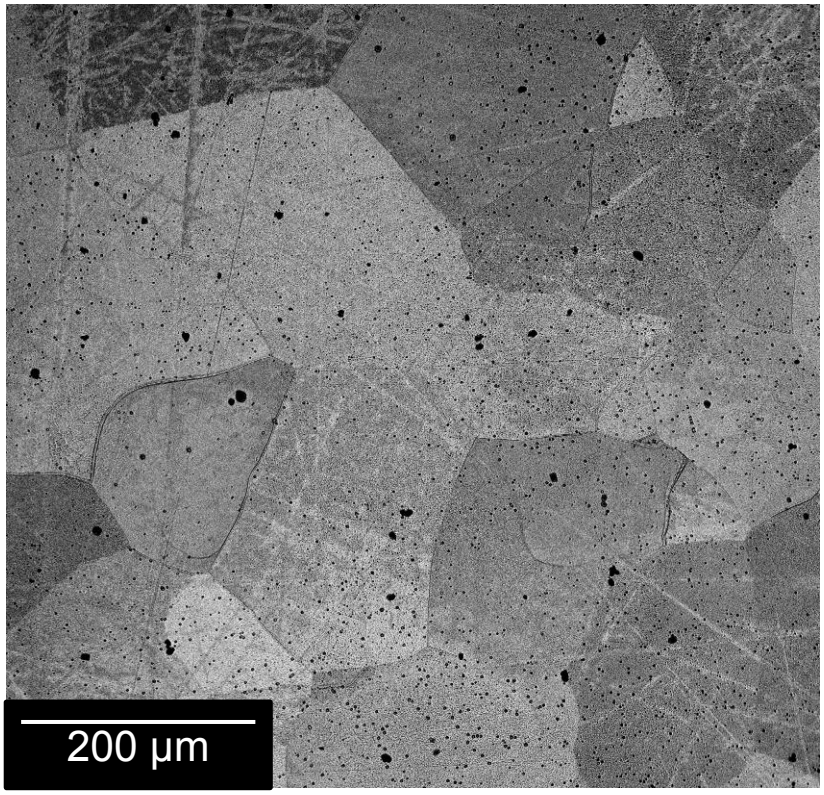

Figure 10: SEM image of the microstructure for a 0% Ni sample.

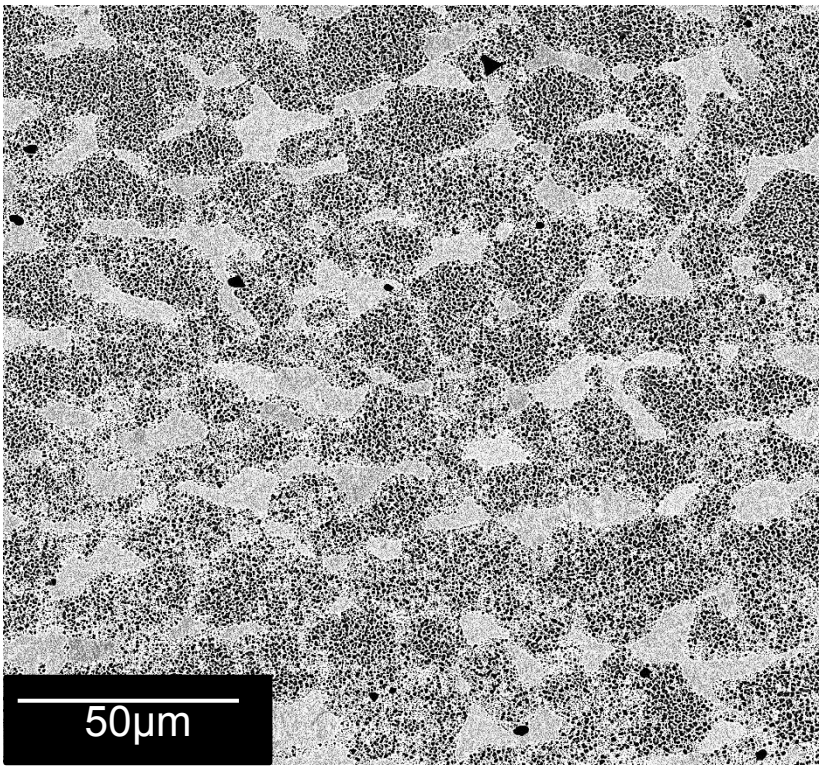

Figure 11: SEM image of the microstructure for a 5% Ni sample.

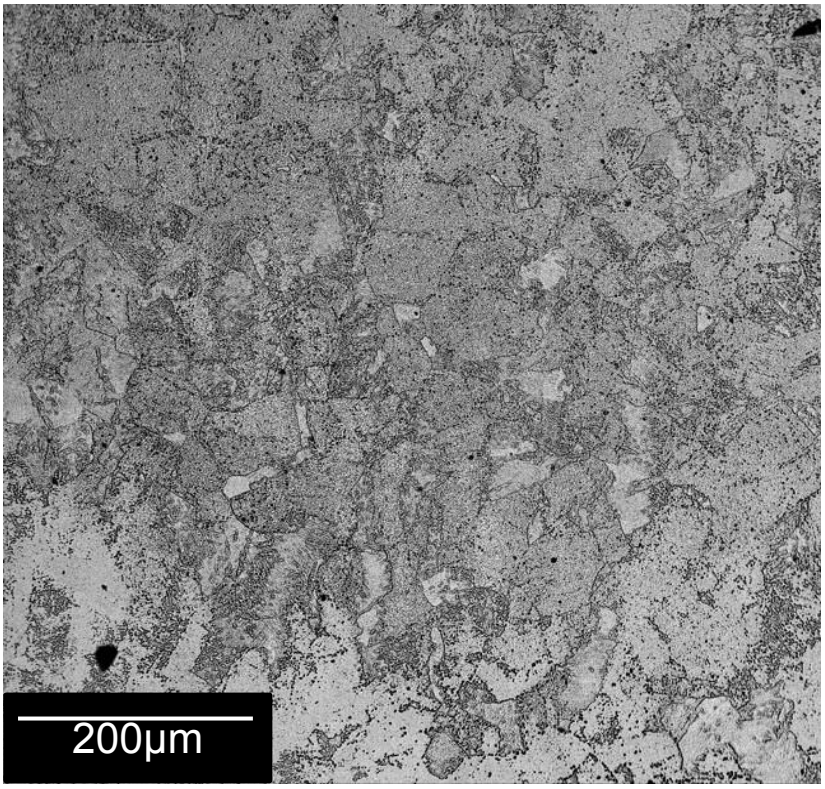

Figure 12: SEM image of the microstructure for a 10% Ni sample.

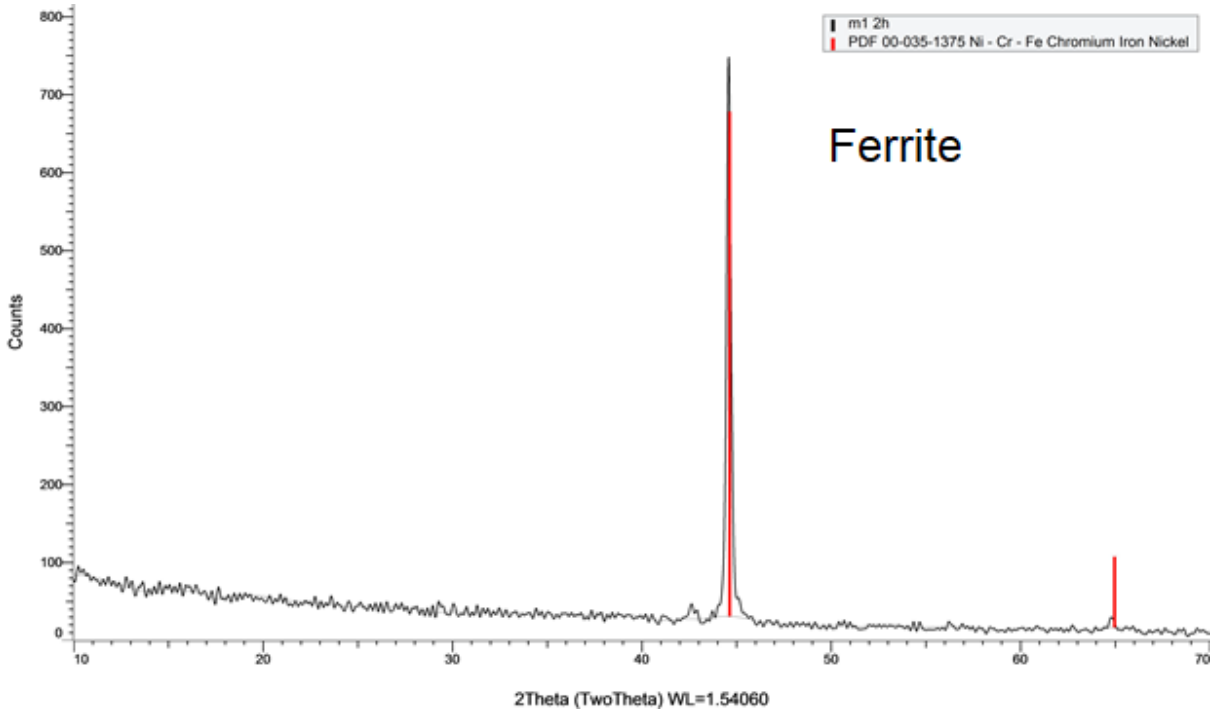

Figure 13: Results from XRD analysis on a 0 % Ni Sample.

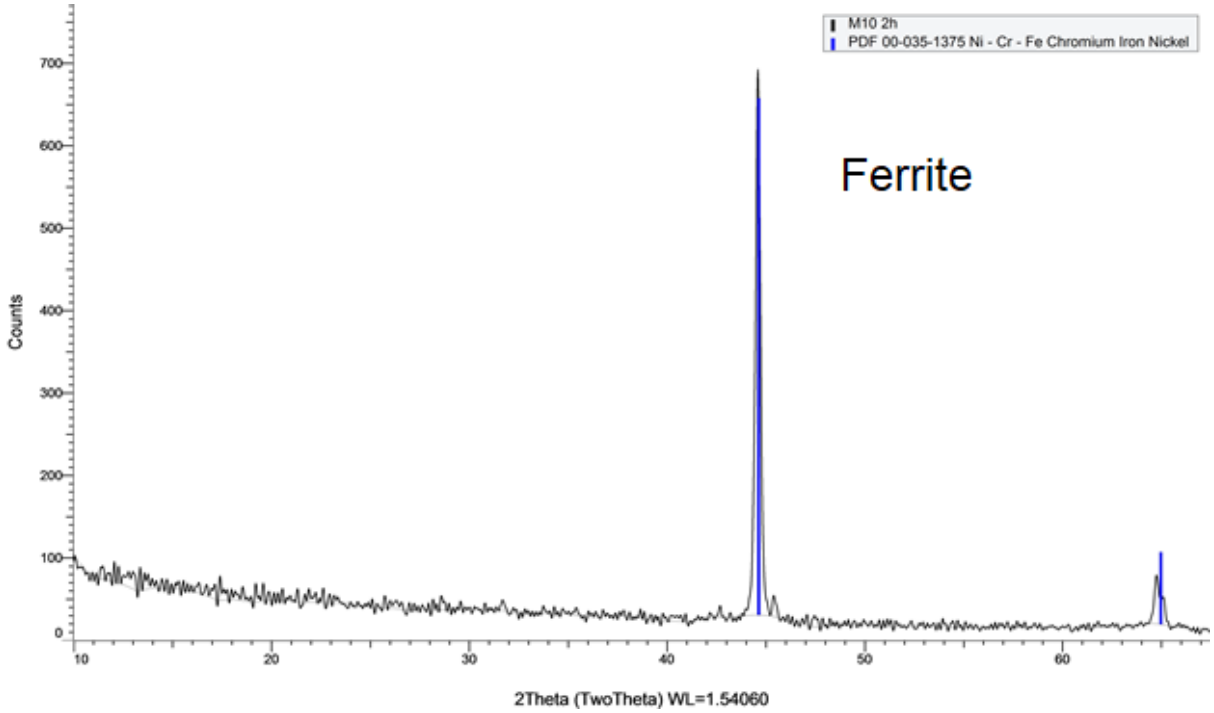

Figure 14: Results from XRD analysis on a 5 % Ni Sample.

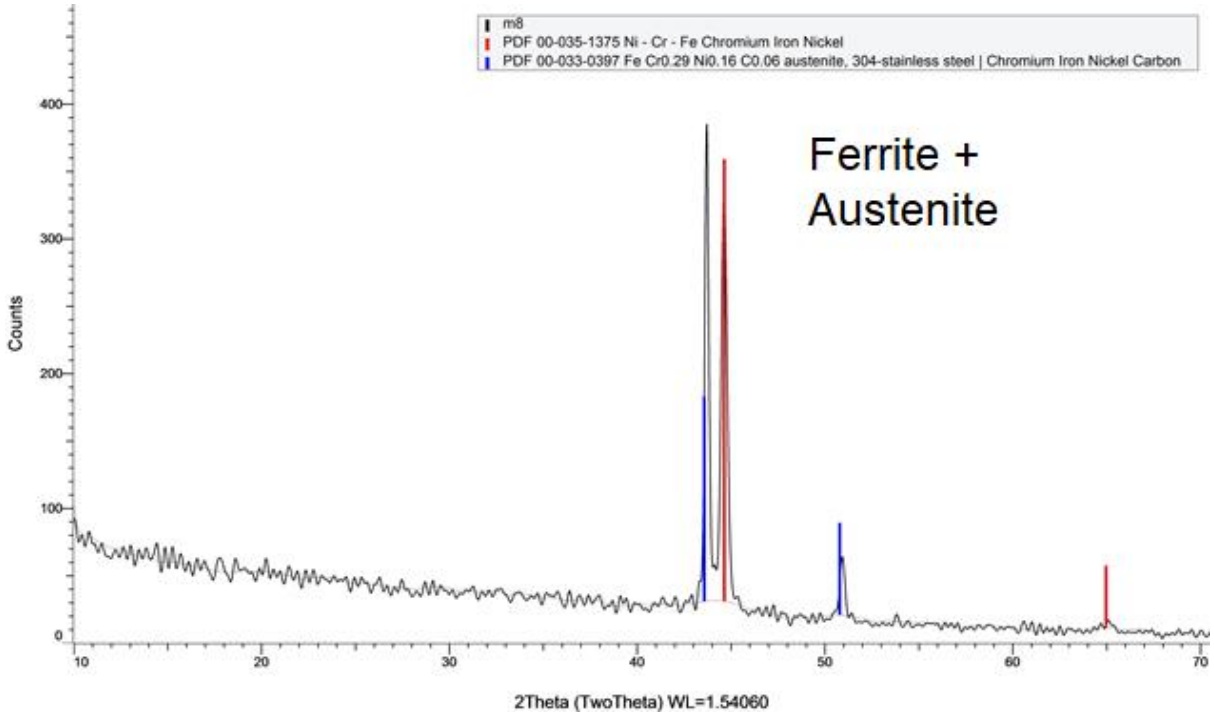

Figure 15: Results from XRD analysis on a 10 % Ni Sample.

Ni	Grain diameter	Phases
0 %	~125-200 µm	Ferrite
5 %	~15-25 µm	Ferrite
10 %	~50-75 µm	Ferrite + Austenite

Table 3: Information about non-exposed samples.

The grain size can be seen to vary between the different model alloys which is worth noting since we know this affects the diffusion and therefore also the corrosion. In the phase diagram, seen in figure 1, the Fe-18Cr-5Ni alloy is close to the ferrite + austenite (δ +γ) phase area, although the respective XRD does not show tendency for an austenite phase to be present this could be further investigated. Similar investigation could also be done for the Fe-18Cr-10Ni alloy as it should show a σ phase according to figure 1.

Exposed samples

Data collected from tube furnace exposures similar to this study but without K_2CO_3 by A. Olivas can be seen in figure 16. These show very low mass gain which indicates that a protective scale has been formed and breakaway has not occurred. This data is useful as a reference for the other exposures.

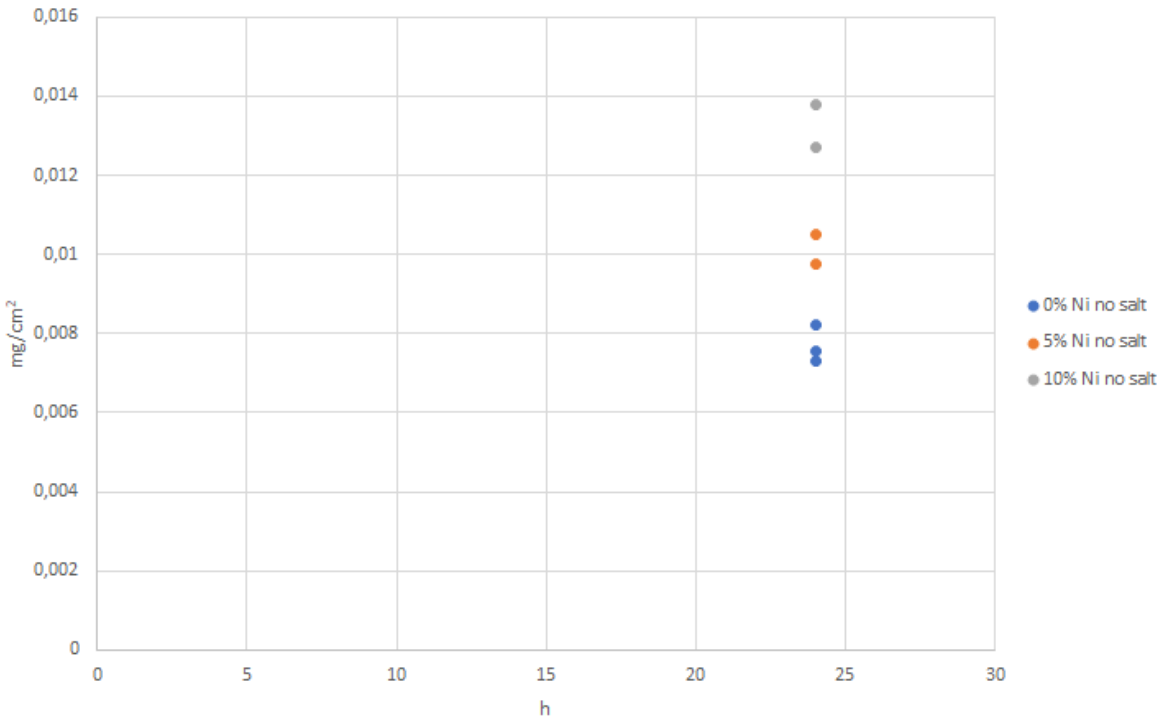

Figure 16: Mass gains for samples exposed for 24h in tube furnace without K_2CO_3. Performed by A. Olivas, Chalmers, Chemistry and Chemical Engineering, Division of Energy and Materials.

The mass change curves acquired with the TG give information about the oxidation rates and behavior of the model alloys when exposed, these curves are shown in figure 17. The 10 % Ni sample can be seen to show less mass gain compared to the 5 % and even more so the 0%. The 5% Ni sample shows more incubation time than the others, this can be connected to the small grain size of this alloy since it enhances diffusion and therefore Cr supply to the surface.

To check the reproducibility of the result an additional TG exposure were performed for the 0% Ni sample and external test data from R. Ambati was also included for comparison, this can be seen in Figure 18.

Oxide thickness was calculated from mass gain values based on pure hematite. The results were plot in figure 19. An oxide thickness of 5 µm was selected to be the target for studying the difference in oxide microstructures. Since the model alloys have different composition they also have different microstructures and oxidation rates, so the time required to obtain this thickness was different for each alloy. The individual times were estimated with the mass gain curves as seen in figure 19.

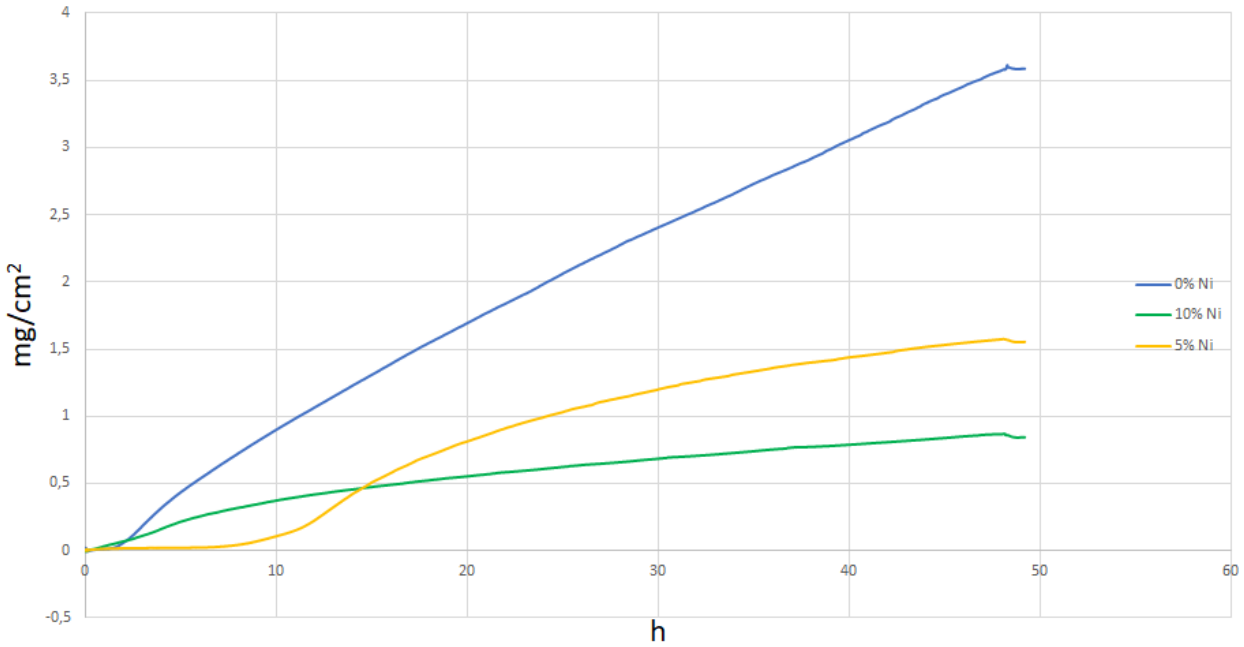

Figure 17: Mass gain curves from TG for 0-10 % Ni samples.

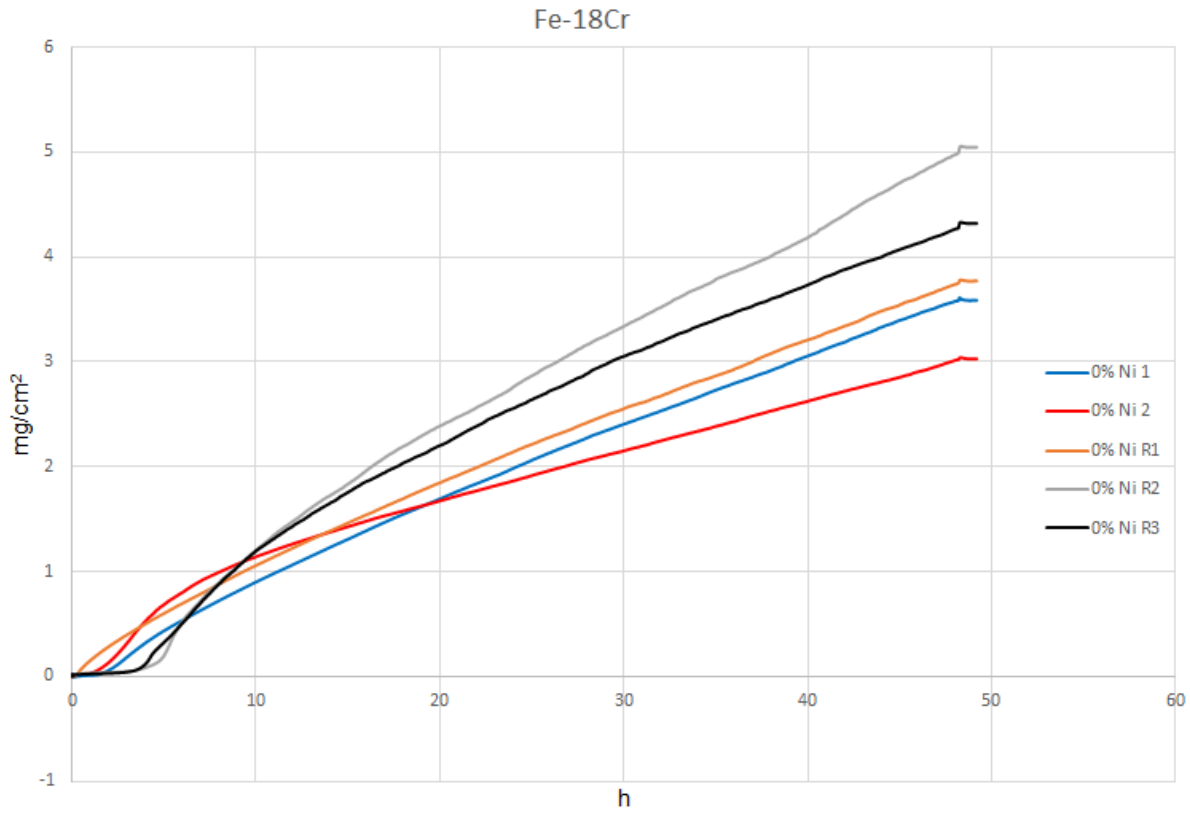

Figure 18: TG mass change curves for 0 % Ni samples. Data Performed by R. Ambati, Chalmers chemistry and chemical engineering division of energy and materials, are marked with R.

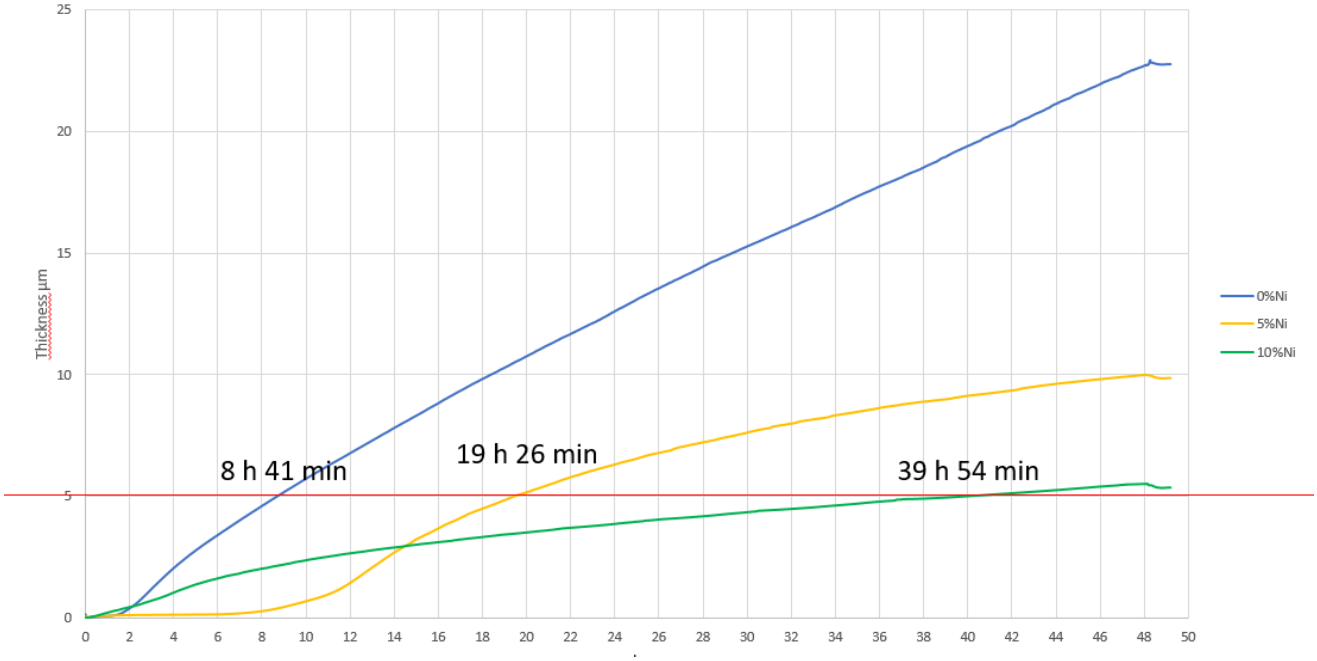

Figure 19: Estimation of exposure time for oxide thickness of 5 µm (hematite) with TG.

The deviation in results are notable for the 0% Ni mass gain curves from figure 18 which show the different mass gains. The R labeled curves show a little incubation time not seen on the others and have more mass gain. The exact reason for this deviation is still not clear, however it is argued that the following factors may have an impact.

- The spraying could generate different deposit evenness
- Grain size or chemical composition may be different in the individual samples
- Precision of the TG
- Sample preparation

Something that also could affect this is the experimental procedure of the one performing the test, however a collaborative test with R. Ambati was performed and no significant difference in preparation could be found. Unfortunately, the TG was malfunctioning and no reliable mass change curve could be generated. It must also be taken into consideration that there could be unknown mechanisms occurring that are affecting the results. To understand more about the reasons for these deviations more pre-exposure analyzes could be performed to check possible individual differences between the samples, e.g. grain size or composition. The exposure times estimated for an equal thickness seen in figure 19 are the ones used for the tube furnace. Tube furnace exposures were performed in order to analyze the oxide microstructure of the different model alloys. In these exposures, the cooling of the samples is considered quick so the oxide microstructure does not have time to change. The results from the tube furnace are plotted in figure 20.

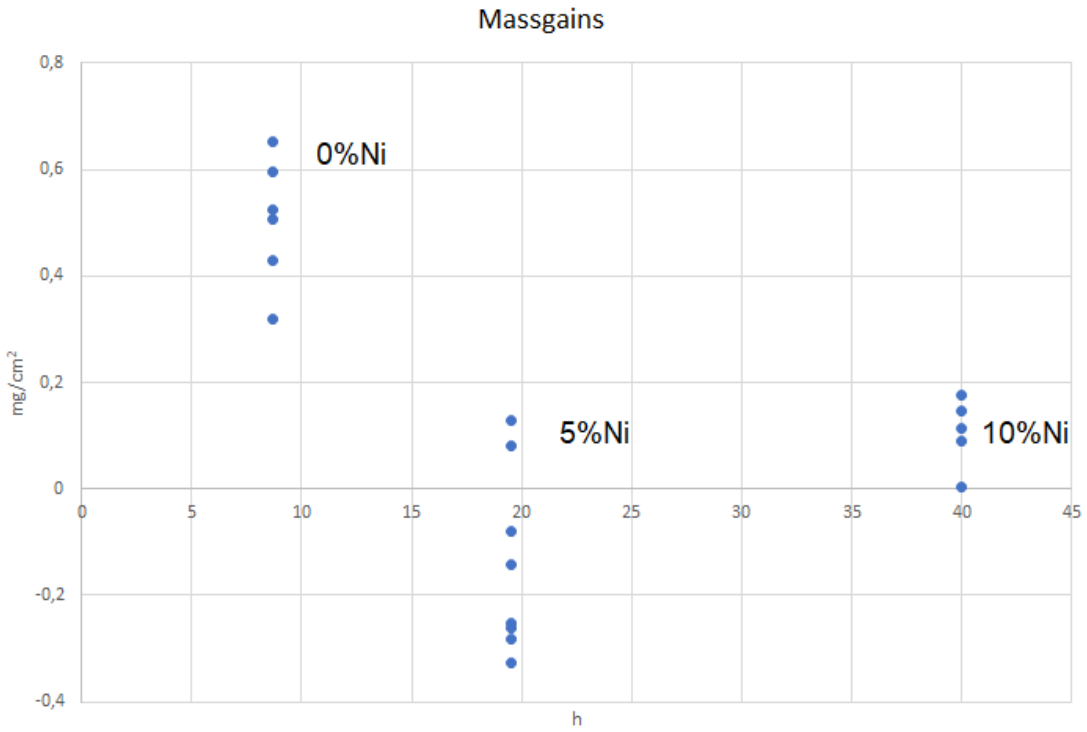

Figure 20: Scatter of the mass gains from the tube furnace samples.

The mass gains from the tube furnace are considerably lower than for the TG and in some cases even negative indicating a mass loss. Although trends for the alloys can be seen in the

scatter of figure 20 so there is reason to believe these results are not bad. The difference in mass gains indicates that replicating TG results with the tube furnace is difficult when choosing an oxide thickness like in this study. The amount of salt deposited on the samples in this study is relatively high and performing a tube exposure requires more contact with the sample compared to TG. This is because the sample is placed in a holder for the tube furnace respective to hanging in a hook for TG, as well as weighing after exposure is needed for the tube furnace samples and not TG. Increased contact makes salt fall off the sample which helps explain the lower mass gain measured for tube furnace samples. The lower gas flow of the TG is a factor that may also affect the mass gain since the higher flow of the tube furnace would be more likely to evaporate the salt which would lead to less measured mass gain for tube exposed samples. The TG also measures the weight continuously which could lead to slightly higher weight since the hot samples weigh more than cold, this can be seen at the very end of TG curves where the heating is turned off. However, this is a relatively small factor which probably have little effect compared to the large differences seen between TG and tube furnace mass gains. The heating of the TG could also be a factor which affects the mass gain since it is cold when started compared to the tube furnace which is pre-heated prior to exposures. This should be taken into consideration for short exposures but at exposure times of 48 hours as used in this study heating should not be a problem and this can be neglected. Regarding the negative mass gains of the 5 % Ni sample one reason could be that the mass gain at the estimated time for the chosen oxide thickness is close to the incubation time seen in figure 19. If the 5 % Ni sample has deviation similar to that seen for the 0 % Ni samples in figure 18 then some samples might not fully pass the incubation time and show considerably lower mass gain.
The spread of points on the scatter is also larger for the lower Ni content alloys which could be expected since figure 19 show higher oxidation rates for these than the 10 % Ni sample at the individual exposure times utilized. The spread of the scatter for the 10 % Ni samples is relatively low which also indicates a stable oxide growth as seen for that alloy in figure 19. If these things are valid the results from figure 19 and 20 should be connectable.

SEM plan view images were also made for the different alloys after TG exposure, these can be seen in figure 21, 22 and 23. The surfaces of the samples after exposure could be identified as covered with a thick Fe-rich oxide as well as with remaining salt, this could be confirmed with the EDX element analysis and the SEM salt image from figure 9.

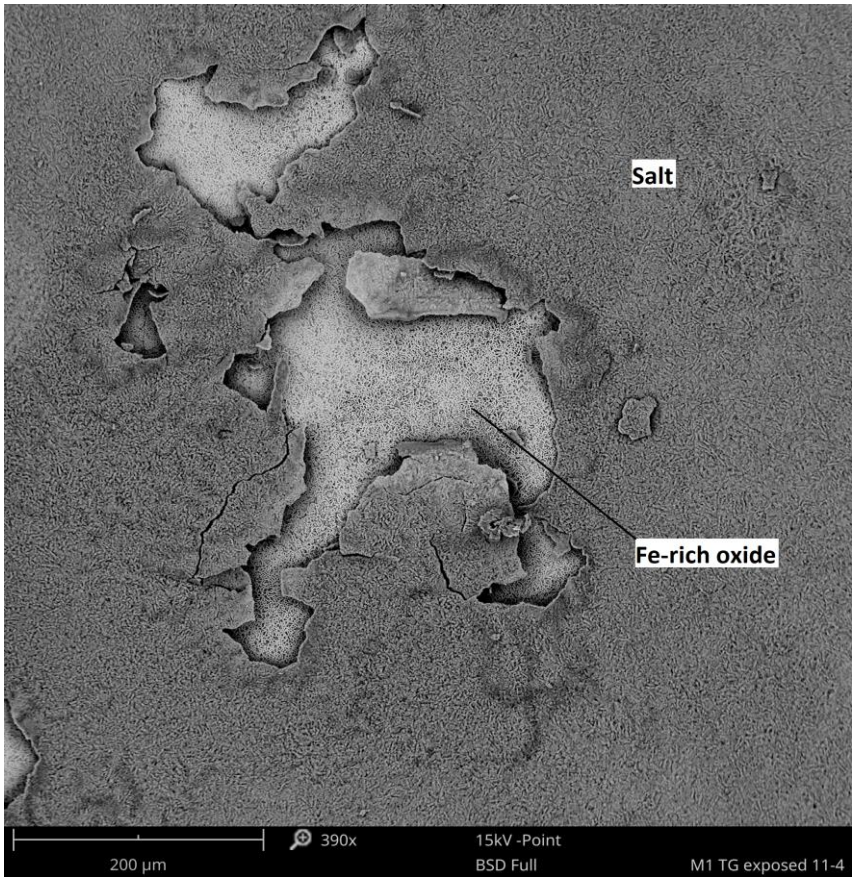

Figure 21: SEM plan view image of a 48 h TG exposed 0 % Ni sample.

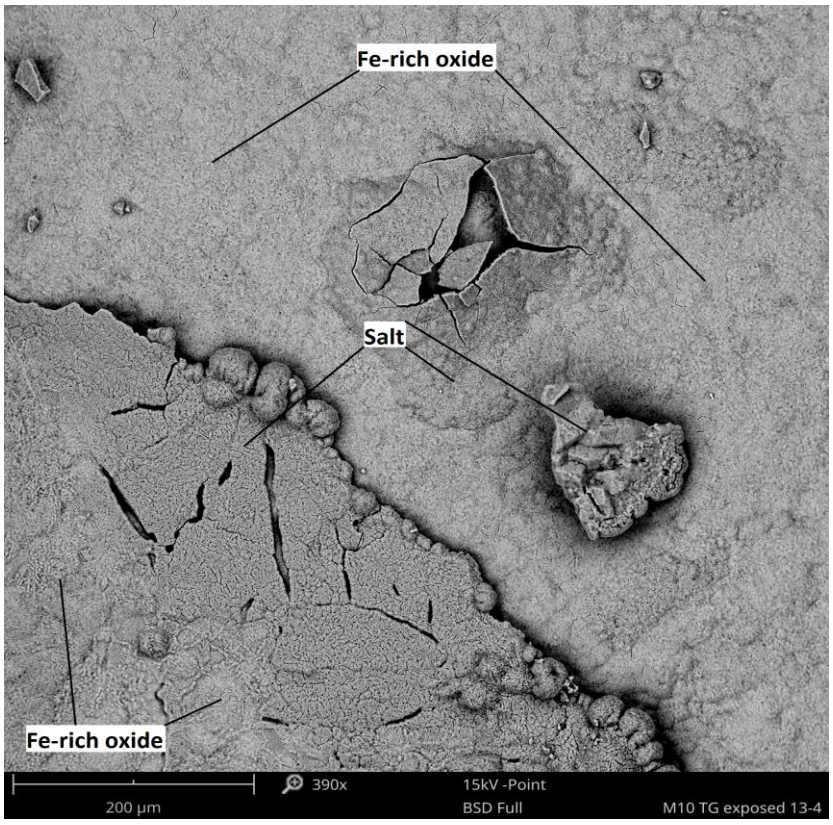

Figure 22: SEM plan view image of a 48 h TG exposed 5 % Ni sample.

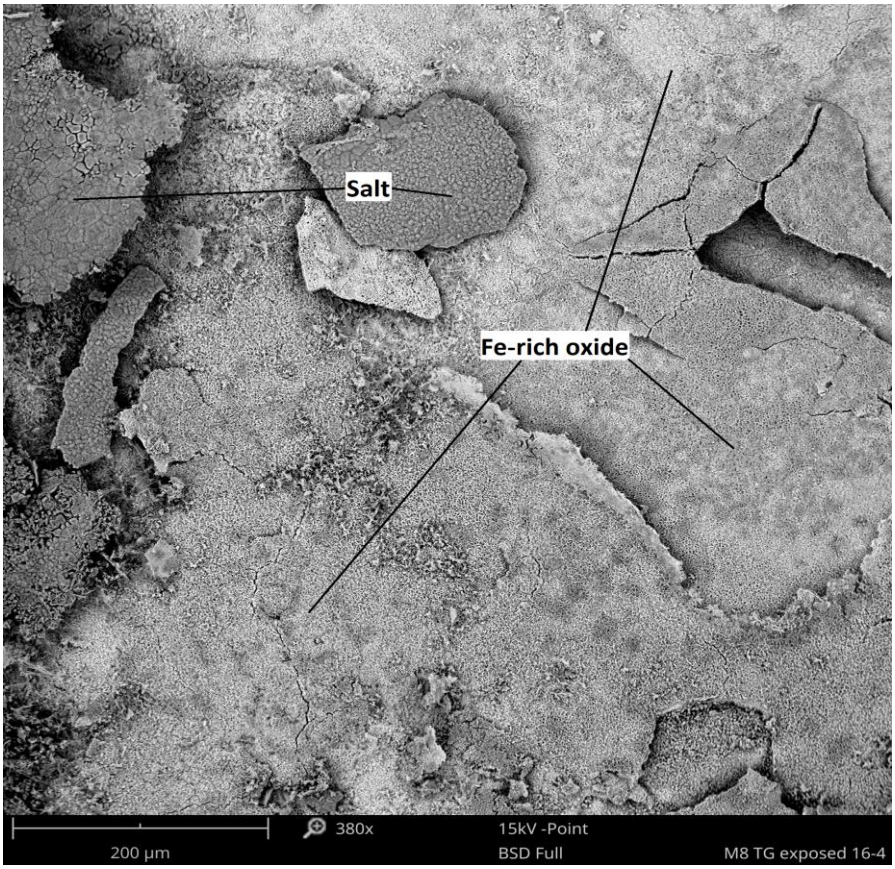

Figure 23: SEM plan view image of a 48 h TG exposed 10 % Ni sample.

Cross section of the 5% Ni alloy was prepared by means of BIB milling and characterized by SEM/EDX analysis. Unfortunately, 0 and 10% Ni alloys were not possible to characterize due to failure of the BIB device. An overview of the cross section is displayed in figure 24 where the covering outwards growing Fe-rich oxide can be seen as well as an inward growing spinel oxide. The salt on top and grains (microstructure) in the metal can also be seen here. The features on figure 24 were identified with EDX analysis. A SEM image of the cross section with associated element mappings gives further information about the oxides and the propagation of the corrosion attack, these can be seen in figure 25.

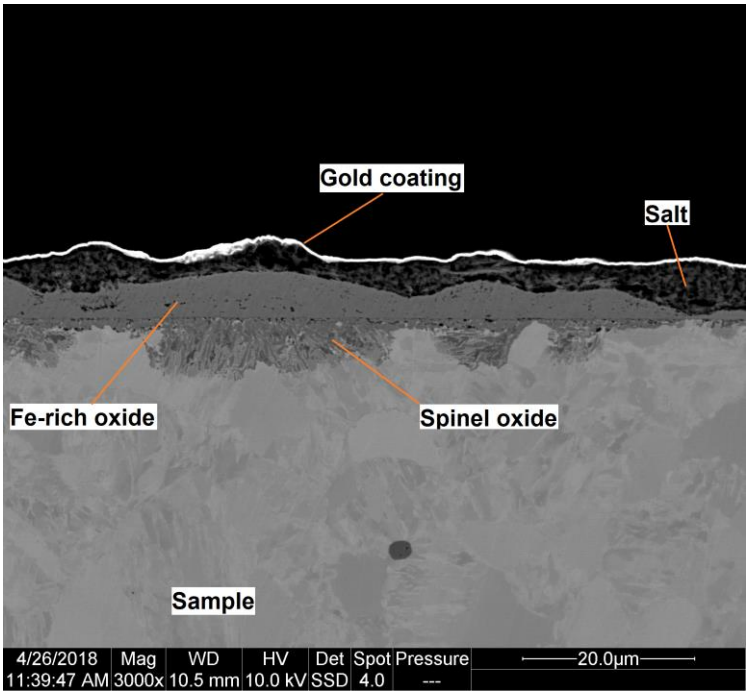

Figure 24: SEM cross section image for a 5 % Ni sample.

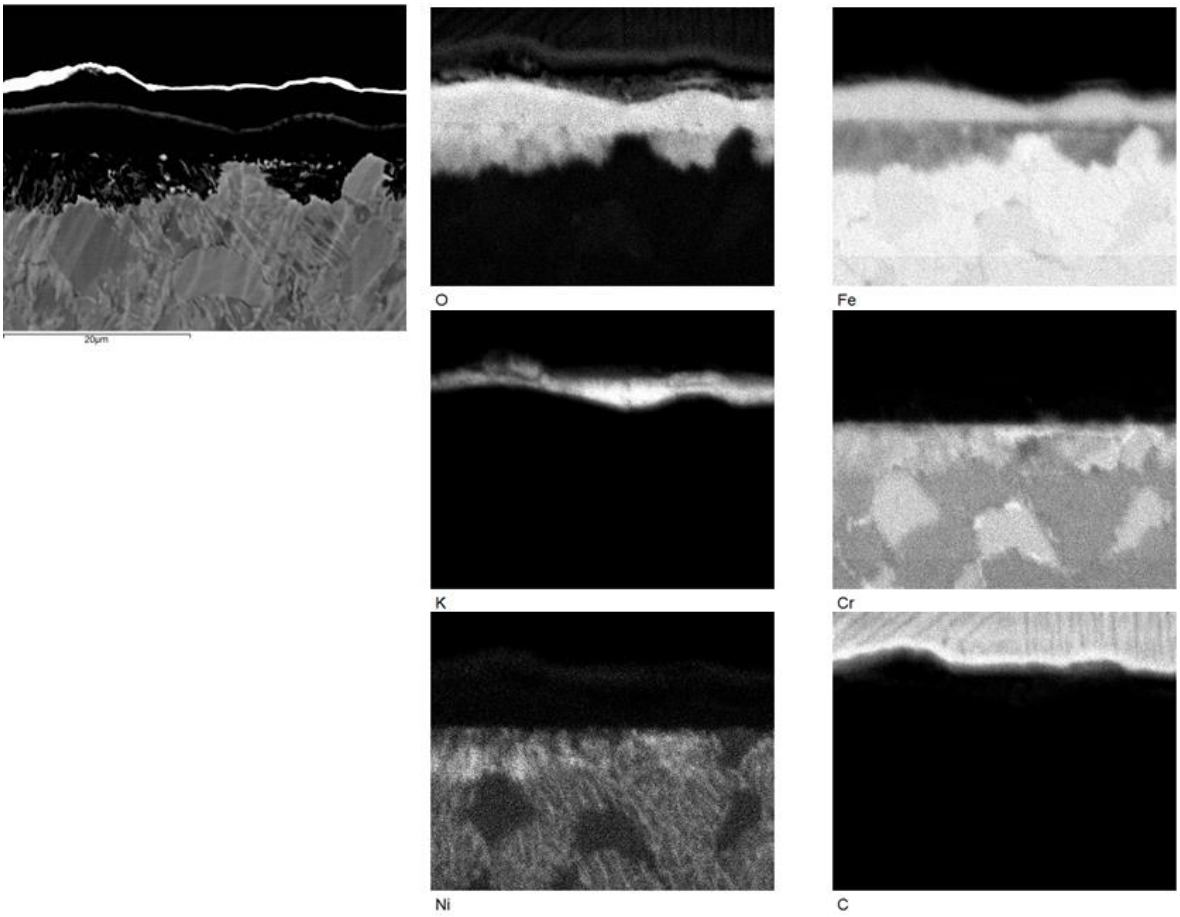

Figure 25: SEM cross section image for a 5 % Ni sample in top left corner with associated element mappings.

Both the suggested outward and inward growing oxides can be confirmed as oxides by the O mapping in figure 25. The outward growing oxide can be seen in the mappings to be rich in Fe but have very little Ni and Cr. The inward growing oxide can be seen to have less Fe than the outward growing but has content of both Ni and Cr, hence this is suggested to be a spinel oxide. In the metal, grains can be distinguished which have lower Ni content (~2.5 %) and slightly higher Cr content. These are likely to be grains with a pure ferrite phase since ferrite does not contain Ni. Since there is a lower amount of Ni in these grains the Ni amount is higher in the phases surrounding them which also can be seen in the mappings. As the Ni content is raised above 5 % in this area the alloy is pushed towards the ferrite + austenite region in the phase diagram (figure 1). Thus, there is reason to believe what surrounds the ferrite grains is a combination of austenite and ferrite even though this contradicts the XRD results for this sample (figure 14). There is conflict in these results but the XRD was performed before exposure and the cross section after so a possible explanation is that austenite could have been formed during the exposure. This is not unlikely since the alloy is close to the ferrite + austenite region in the phase diagram for the exposure temperature. To further investigate this an XRD could be performed on exposed samples to gain more information about the behavior of the metal under exposure. The K mapping shows that there is still salt on top of the Fe-rich oxide.

External results

As the 0 % and 10% Ni model alloys could not be milled in the BIB there is no cross section for them to be shown for comparison. There is however cross section analyzes for alloys with composition and exposures similar to this study in the literature. Replacing the 0 % Ni model alloy of this study is a similar model alloy that was exposed in a different environment for 168 hours done by B Pujilaksono, et al, this can be seen in figure 26 [36]. This exposure uses water vapor which has similar effect as K_2CO_3 and consumes Cr by reacting and leading to $CrO_2(OH)_2$ vaporization, which should make the results comparable to the ones from this study [29]. A cross section for the 10 % Ni model alloy of this study is replaced by an image of the austenitic commercial steel 304L exposed for 168 hours done by T Jonsson, et al. This steel has the same amounts of Cr and Ni as the model alloy, the exact composition can be seen in table 4 and the cross section in figure 27 [37]. This exposure for this sample was performed with 0.1 mg/cm^2 K_2CO_3 for 168h.

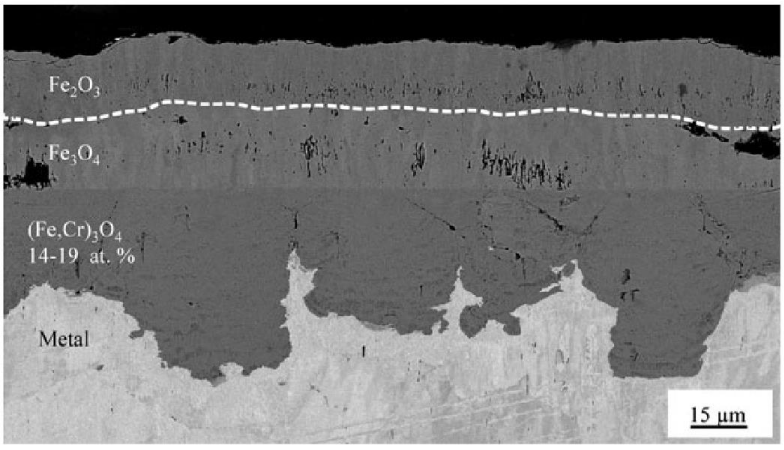

Figure 26: Cross section of a Fe-18Cr model alloy exposed in wet O_2 at 600°C for 168h made by B Pujilaksono [36].

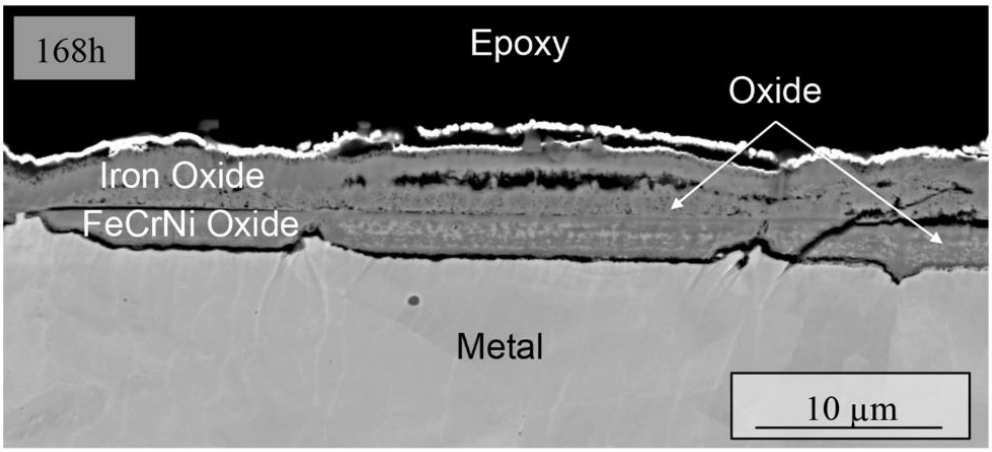

Figure 27: Cross section of a 304L commercial steel (18Cr-10Ni) exposed in O_2 + 0.1 mg/cm^2 K_2CO_3 at 600°C for 168h made by T Jonsson [37].

Element	Fe	Cr	Ni	Mn	Si	Mo
18Cr–10Ni	Bal.	18.5	10.2	1.41	0.55	0.49

Table 4: Composition of the 304L commercial steel.

By assuming these cross sections are comparable with the one shown in this study (Figure 24) information can be gained about the morphology of the oxides when the Ni content is changing. The 304L steel cross section in figure 27 shows a homogeneous oxide growth not seen for the steels with lower Ni content in figures 24 and 26. Since this is the only steel with an austenitic phase it could be argued that this phase contributes to this behavior. It should however be noted that this steel also has content of other elements which may contribute to this effect. The effect of grain boundaries being diffusion paths for Cr are clear for the 304L cross section as well where both oxides can be seen growing less around the boundaries. The homogeneous oxide growth of austenite can also be argued visible for the 5 % Ni sample in the spinel seen in figure 24. If assuming the previously argued phases for this alloy, the spinel oxide seems to be growing around the ferrite grains and evenly inwards through the austenite + ferrite phase which would then support what was discussed about the 304L. The size of the austenitic grains in these two alloys are hard to discuss since the 5 % Ni model alloy does not show any distinguishable grains in the same sense as the 304L. Comparison between the 0 % and 5 % Ni samples is hard since the differences between these are not as clear as the ones seen for 304L. Since the exposure time plays an important role for the oxide growth and the difference between the two exposure times are so big a fair assessment cannot be made for the difference in oxide microstructures.

In a study by R. Peraldi and B.A. Pint different Fe-Cr-Ni model alloys were exposed in an environment of 10 % water vapor at 650°C and 800°C for a total of 100 hours in order to study the oxide scales formed [15]. Two model alloys which are used in this study are also included in the article (Fe-18Cr and Fe-18Cr-10Ni). The results from the exposures done in the article are shown in figure 28.

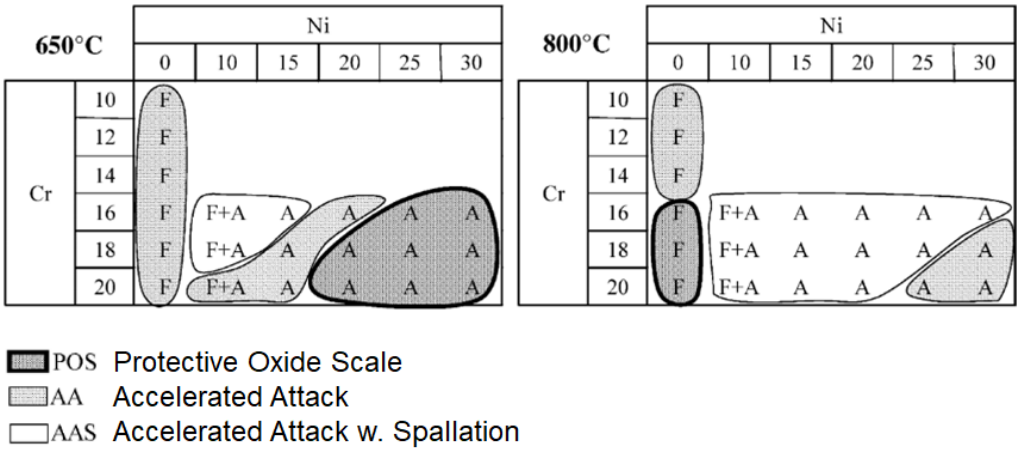

Figure 28: Exposure results by R. Peraldi and B.A. Pint showing oxide scale behavior of Fe-Cr-Ni model alloys [15].

The austenitic alloys are stated to show better corrosion resistance at the lower temperature and the ferritic ones better at the higher temperature. At 600-650°C the calculated Cr diffusion was similar for the phases which suggested a beneficial effect of Ni in resistance to water vapor since the austenitic alloys performed better at this temperature and environment in that study. However, the of the austenitic alloys showed inferior performance to the ferritic alloys at 800°C. The breakaway on ferritic alloys is stated to be delayed at higher temperature while the growth of protective oxide was reduced for austenitic alloys. The addition of either Cr or Ni is also stated to delay the onset of an accelerated attack. The positive effect of Ni on the corrosion resistance of the article agrees with the results acquired in this study. Based on this, the behavior of Fe-Cr-Ni model alloys can then be argued to be similar for water vapor and K_2CO_3 environments. Though, it should be noted that the results from the article are acquired from oxide scale behavior while the results from this study are based on mass gains. Judging from the SEM images for the common alloys of this article (figure 21 and 23) the exact same behavior cannot be distinguished as presented in figure 28, i.e. spallation on the Fe-18Cr-10Ni alloy. The reason for this could be that the shorter exposure times used for the SEM plan views in this study is not enough to show the same behavior as in the article which utilizes a total of 100 h exposures compared to 48 h.

Conclusion

A conclusion that can be drawn from this study is that the addition of Ni to a Fe-18Cr alloy gives positive effects on corrosion resistance when exposed in aggressive environments at temperatures around 600°C. For the composition range of this study the samples show lower mass gain with increasing amounts of Ni. An incubation time is seen for the 0 % and 5 % Ni samples in TG exposures but seemingly this is effect is not present for the 10 % Ni sample which also indicates a positive effect of Ni. The long incubation for the 5 % Ni samples is considered caused by the small grain size of this alloy. Choosing an oxide thickness for analyzing and comparison showed to be hard when attempting to replicate TG results with the tube furnace since a deviation can be seen in the results acquired with both exposure methods. If an oxide thickness is chosen for this purpose or as an equal starting point for further exposures, e.g. secondary exposure with different environment, factors discussed in this study should be taken into consideration. Choosing an oxide thickness where the alloys have well passed their incubation time should be beneficial as the deviation otherwise puts the alloys in risk of showing very little mass gain in case they do not pass the incubation time. This effect also leads to greater difference in mass gains if some of the samples pass the incubation and some do not. These effects were seen for the 5 % Ni alloy.

Judging from the cross sections, the oxide microstructure also seems dependent on the phases of the alloy. Alloys can be argued to have a more homogeneous oxide growth in the regions where the austenite phase is present compared to the ferritic regions, this effect was the most visible for the 304L (10% Ni) steel but arguably also for the 5% Ni model alloy. Positive effects are seen for increasing Ni content however this can only be confirmed for exposure temperatures around 600°C. At 800°C Ni has negative effect on the corrosion resistance due to the temperature dependent performance of austenite as stated in the study by R. Peraldi and B.A. Pint [15]. Exactly at what temperature austenitic alloys start performing worse than ferritic cannot be determined but it is within the temperature range of 650-800°C. This should be kept in mind when choosing a steel for a waste fired boiler since the performance can be confirmed to be temperature dependent by that study.

Acknowledgements

This work was carried out within the High Temperature Corrosion Centre (HTC) at Chalmers University of Technology and with support from VINNOVA, Sweden's Innovation Agency, within the Metallic Materials programme.

Special thanks to Andrea Olivas and Torbjörn Jonsson, who have been supervisors for this thesis, for their guidance and knowledge. Also thanks to Johan Eklund, Julien Phother, Sedigheh Bigdeli, Ramu Ambati, Tommy Sand, Douglas Ollhage and Carl Laurell for their help.

References

[1]
Tillman, D. A. (2000). Biomass cofiring: the technology, the experience, the combustion consequences. *Biomass and Bioenergy*, *19*(6), 365-384.

[2]
Haanappel, V. A. C., Fransen, T., & Gellings, P. J. (1992). Chlorine-induced high temperature corrosion: I. Metals and alloys-A review. *High temperature materials and processes*, *10*(2), 67-90.

[3]
Davidsson K.O et al. Potassium, C. Sulfur in Ash, Particles, Deposits, and Corrosion during Wood Combustion in a Circulating Fluidized-Bed Boiler. Energy and fuels 2007. 21(1): p.71-81.

[4]
Nielsen, H. P., Frandsen, F. J., Dam-Johansen, K., & Baxter, L. L. (2000). The implications of chlorine-associated corrosion on the operation of biomass-fired boilers. *Progress in energy and combustion science*, *26*(3), 283-298.

[5]
Michelsen, H. P., Frandsen, F., Dam-Johansen, K., & Larsen, O. H. (1998). Deposition and high temperature corrosion in a 10 MW straw fired boiler. *Fuel processing technology*, *54*(1-3), 95-108.

[6]
Jenkins, B., Baxter, L. L., Miles Jr, T. R., & Miles, T. R. (1998). Combustion properties of biomass. *Fuel processing technology*, *54*(1-3), 17-46.

[7]
Pettersson, J., Asteman, H., Svensson, J. E., & Johansson, L. G. (2005). KCl induced corrosion of a 304-type austenitic stainless steel at 600 C; the role of potassium. *Oxidation of Metals*, *64*(1-2), 23-41.

[8]
Pettersson, J., Folkeson, N., Johansson, L. G., & Svensson, J. E. (2011). The effects of KCl, K 2 SO 4 and K 2 CO 3 on the high temperature corrosion of a 304-type austenitic stainless steel. *Oxidation of metals*, *76*(1-2), 93-109.

[9]
Easterly, J. L., & Burnham, M. (1996). Overview of biomass and waste fuel resources for power production. *Biomass and Bioenergy*, *10*(2-3), 79-92.

[10]
Halvarsson, M., Tang, J. E., Asteman, H., Svensson, J. E., & Johansson, L. G. (2006). Microstructural investigation of the breakdown of the protective oxide scale on a 304 steel in the presence of oxygen and water vapour at 600 C. *Corrosion Science*, *48*(8), 2014-2035.

[11]
Jonsson, T., Karlsson, S., Hooshyar, H., Sattari, M., Liske, J., Svensson, J. E., & Johansson, L. G. (2016). Oxidation after breakdown of the chromium-rich scale on stainless steels at high temperature: internal oxidation. *Oxidation of Metals*, *85*(5-6), 509-536.

[12]
Pettersson, J., Folkeson, N., Johansson, L. G., & Svensson, J. E. (2011). The effects of KCl, K 2 SO 4 and K 2 CO 3 on the high temperature corrosion of a 304-type austenitic stainless steel. *Oxidation of metals*, *76*(1-2), 93-109.

[13]
Callister Jr, W.D.,Materials Science and Engineering: An introduction, 5th edn.,John Wiley & Sons, New York, (1999)

[14]
Jonsson, T. (2018). *Materiallära K3*. Göteborg: Chalmers.

[15]
Peraldi, R., & Pint, B. A. (2004). Effect of Cr and Ni contents on the oxidation behavior of ferritic and austenitic model alloys in air with water vapor. *Oxidation of metals*, *61*(5-6), 463-483.

[16]
Jonsson, T. (2018). *Materiallära M2*. Göteborg: Chalmers.

[17]
Thermocalc.com. (2018). *Thermo-Calc Software - Computational Materials Engineering*. [online] Available at: http://www.thermocalc.com/ [Accessed 10 May 2018].

[18]
Jones, D.A, *Principles and Preventions of Corrosion.* 1992, New York Macmillan.

[19]
Petterson J. Alkali induced high temperature corrosion of stainless steel. Göteborg: Chalmers University of Technology; 2008.

[20]
Birks, N., Meier, G. and Pettit, F. (n.d.). *Introduction to the High Temperature Oxidation of Metals*. 2nd ed. Cambridge: Cambridge University Press.

[21]
Jonsson, T. (2018). *Materiallära K4*. Göteborg: Chalmers.

[22]
Kofstad, P., High Temperature Corrosion. 1988, London: Elsevier Applied Science.

[23]
Callister, W.D. and D.G. Rethwisch, *Materials science and engineering: an introduction.* 2010: Wiley

[24]
Nde-ed.org. (2018). *Crystal Defects - Linear Defects (Dislocations)*. [online] Available at: https://www.nde-ed.org/EducationResources/CommunityCollege/Materials/Structure/linear_defects.htm [Accessed 28 May 2018].

[25]
Atkinson, A. and R.I. Taylor, *The diffusion of Ni in the bulk and along dislocations in NiO single crystals.* Philosophical magazine A, 1979.39(39): p. 581-595.

[26]
R. Peraldi, and B. A. Pint, Oxidation of Metals, in preparation.

[27]
Jones, D.A., *Principles and Prevention of corrosion.* 1992, New Jersey: Prentice hall.

[28]
Wagner, C., *Beitrag zur Theorie des Anluafvorgangs.* Z.Physicalshe Chemie,1933. B21: p. 25-42.

[29]
Barin, I. (1995). Thermodynamic data of pure substances, VCH verlagsgeserschaft mbH.

[30]
Jonsson, T., Froitzheim, J., Pettersson, J., Svensson, J.-E., Johansson, L.-G.,Halvarsson, M., The Influence of KCl on the Corrosion of an Austenitic Stainless Steel (304L) in Oxidizing Humid Conditions at 600 degrees C: A Microstructural Study.Oxidation of Metals , (2009),73(3–4), pp. 213–239.

[31] TGA, S. and Instrumentation, S. (2018). *SETSYS Evolution TGA: Thermogravimetric Analyzer TGA - Setaram*. [online] Setaram.com. Available at: http://www.setaram.com/setaram-products/thermal-analysis/thermogravimetry-tga/setsys-evolution-tga [Accessed 5 May 2018].

[32] Techniques. (2018). *Scanning Electron Microscopy (SEM)*. [online] Available at: https://serc.carleton.edu/research_education/geochemsheets/techniques/SEM.html [Accessed 6 May 2018].

[33] Zhou, W. and Wang, Z. (2007). *Scanning microscopy for nanotechnology*. New York: Springer.

[34]
Chalmers.se. (2015). Leica EM TIC 3X. Available at: https://www.chalmers.se/en/researchinfrastructure/CMAL/instruments/FIB/BIB/Pages/Leica-TIC-3X.aspx [Accessed 7 May 2018].

[35] Santiago Rivera, M. (2006). Operating the Siemens XRD Diffraktometer D5000. Mayaguez: University of Puerto Rico. Available at: http://geology.uprm.edu/facilities/xrdforms/SOP-Siemens-XRD-Diffraktometer-D5000.pdf

[36]
Pujilaksono, B. (2008). *The effect of watervapor on the high temperature corrosion properties of pure chromium, pure iron and four Fe-Cr alloys*. Göteborg: Chalmers university of Technology.

[37]
Jonsson, T., Karlsson, S., Hooshyar, H., Sattari, M., Liske, J., Svensson, J. E., & Johansson, L. G. (2016). Oxidation after breakdown of the chromium-rich scale on stainless steels at high temperature: internal oxidation. *Oxidation of Metals*, *85*(5-6), 509-536.